ISBN 978-82-471-2494-9 (printed ver.)
ISBN 978-82-471-2495-6 (electronic ver.)
ISSN 1503-8181

George K. El Khoury
Doctoral Thesis

Doctoral theses at NTNU, 2011:5

George K. El Khoury

Numerical simulations of massively separated turbulent flows

NTNU
Norwegian University of
Science and Technology
Thesis for the degree of
philosophiae doctor
Faculty of Engineering Science and Technology
Department of Marine Technology

NTNU
Norwegian University of
Science and Technology

Doctoral theses at NTNU, 2011:5

NTNU

NTNU
Norwegian University of
Science and Technology

George K. El Khoury

Numerical simulations of massively separated turbulent flows

Thesis for the degree of philosophiae doctor

Trondheim, January 2011

Norwegian University of
Science and Technology
Faculty of Engineering Science and Technology
Department of Marine Technology

NTNU
Norwegian University of
Science and Technology

NTNU
Norwegian University of Science and Technology

Thesis for the degree of philosophiae doctor

Faculty of Engineering Science and Technology
Department of Marine Technology

ISBN 978-82-471-2494-9 (printed ver.)
ISBN 978-82-471-2495-6 (electronic ver.)
ISSN 1503-8181

Doctoral Theses at NTNU, 2011:5

Printed by Tapir Uttrykk

Numerical simulations of massively separated turbulent flows.

George K. El Khoury 2010
Department of Marine Technology, NTNU
NO-7491 Trondheim, Norway.

Abstract

It is well known that most fluid flows observed in nature or encountered in engineering applications are turbulent and involve separation. Fluid flows in turbines, diffusers and channels with sudden expansions are among the widely observed areas where separation substantially alters the flow field and gives rise to complex flow dynamics. Such types of flows are referred to as internal flows since they are confined within solid surfaces and predominantly involve the generation or utilization of mechanical power. However, there is also a vast variety of engineering applications where the fluid flows past solid structures, such as the flow of air around an airplane or that of water around a submarine. These are called external flows and as in the former case the downstream evolution of the flow field is crucially influenced by separation.

The present doctoral thesis addresses both internal and external separated flows by means of direct numerical simulations of the incompressible Navier-Stokes equations. For internal flows, the wall-driven flow in a one-sided expansion channel and the pressure-driven flow in a plane channel with a single thin-plate obstruction have been studied in the fully developed turbulent state. Since such geometrical configurations involve spatially developing turbulent flows, proper inflow conditions are to be employed in order to provide a realistic fully turbulent flow at the input. For this purpose, a newly developed technique has been used in order to mimic an infinitely long channel section upstream of the expansion and the obstruction, respectively. With this approach, we are able to gather accurate mean flow and turbulence statistics throughout each flow domain and to explore in detail the instantaneous flow topology in the separated shear layers, recirculation regions as well as the recovery zones.

For external flows, on the other hand, the flow past a prolate spheroid has been studied. Here, a wide range of Reynolds numbers is taken into consideration. Based on the characteristics of the vortical structures in the wake, the flow past a prolate spheroid is classified as laminar (steady or unsteady), transitional or turbulent. In each flow regime, the characteristic features of the flow are investigated by means of detailed frequency analysis, instantaneous vortex topology and three-dimensional flow visualizations.

Descriptors: Direct numerical simulations, incompressible flows, separation, turbulent inflow conditions, wall-bounded flows, sudden expansion flows, obstructed flows, bluff body flows, prolate spheroid.

Preface

This thesis is divided into two main parts. The first part consists of an introduction and a brief review of the main results obtained. The second part includes the papers and is divided into two sections: wall-bounded flows and bluff body flows.

The work on wall-bounded flows was in collaboration with the Department of Energy and Process Engineering at NTNU where MB was a PhD student at that time. BP and HIA supervised the work and assisted in the analysis and interpretation of the findings and in the writing process.

The thesis is based on and contains the following papers.

Paper 1. Barri, M., El Khoury, G. K., Andersson, H. I. & Pettersen, B. 2009 Inflow conditions for inhomogeneous turbulent flows. *Int. J. Numer. Meth. Fluids* **60**, 227–235.

Paper 2. El Khoury, G. K., Andersson, H. I., Barri, M. & Pettersen, B. 2010 Massive separation of turbulent Couette flow in a one-sided expansion channel. *Int. J. Heat. Fluid Flow* **31**, 274–283.

Paper 3. El Khoury, G. K., Pettersen, B., Andersson, H. I. & Barri, M. 2010 Asymmetries in an obstructed turbulent channel flow. *Phys. Fluids* **22**, 095103–13.

Paper 4. El Khoury, G. K., Andersson, H. I. & Pettersen, B. 2010 Wakes behind a prolate spheroid in crossflow. *J. Fluid Mech.* submitted.

Paper 5. El Khoury, G. K., Andersson, H. I. & Pettersen, B. 2010 Crossflow past a prolate spheroid at Reynolds number of 10 000. *J. Fluid Mech.* **659**, 365–374.

List of Publications

Journal Papers

Paper 1. El Khoury, G. K., Andersson, H. I. & Pettersen, B. 2009 Simulating turbulent Dean flow in Cartesian coordinates. *Int. J. Numer. Meth. Fluids* **60**, 263–274.

Paper 2. Barri, M., El Khoury, G. K., Andersson, H. I. & Pettersen, B. 2009 Inflow conditions for inhomogeneous turbulent flows. *Int. J. Numer. Meth. Fluids* **60**, 227–235.

Paper 3. Barri, M., El Khoury, G. K., Andersson, H. I. & Pettersen, B. 2010 DNS of backward-facing step flow with fully turbulent inflow. *Int. J. Numer. Meth. Fluids* **64**, 777–792.

Paper 4. El Khoury, G. K., Andersson, H. I., Barri, M. & Pettersen, B. 2010 Massive separation of turbulent Couette flow in a one-sided expansion channel. *Int. J. Heat. Fluid Flow* **31**, 274–283.

Paper 5. El Khoury, G. K., Pettersen, B., Andersson, H. I. & Barri, M. 2010 Asymmetries in an obstructed turbulent channel flow. *Phys. Fluids* **22**, 095103–13.

Paper 6. El Khoury, G. K., Andersson, H. I. & Pettersen, B. 2010 Wakes behind a prolate spheroid in crossflow. *J. Fluid Mech.* submitted.

Paper 7. El Khoury, G. K., Andersson, H. I. & Pettersen, B. 2010 Crossflow past a prolate spheroid at Reynolds number of 10 000. *J. Fluid Mech.* **659**, 365–374.

Conference Papers

Paper 1. El Khoury, G. K., Barri, M., Andersson, H. I. & Pettersen, B. 2008 DNS of orifice flow with turbulent inflow conditions. *ERCOFTAC workshop, Direct and Large-eddy simulation (DLES-7).* Trieste-Italy, September 8-10, 2008.

Paper 2. El Khoury, G. K., Barri, M., Andersson, H. I. & Pettersen, B. 2009 Massive separation of turbulent Couette flow in a one-sided expansion channel. *The* 6^{th} *International Symposium on Turbulence and Shear Flow Phenomena (TSFP-6).* Seoul-Korea, June 22-24, 2009.

Paper 3. Barri, M., El Khoury, G. K., Andersson, H. I. & Pettersen, B. 2009 Massive separation in rotating turbulent flows. *European turbulence conference ETC-12.* Marburg-Germany, September 7-10, 2009.

Paper 4. Gallardo, J. P., El Khoury, G. K., Pettersen, B. & Andersson, H. I. 2010 Flow past a curved circular cylinder in uniform shear at Reynolds number of 500. *The* 8^{th} *International ERCOFTAC Symposium on Engineering Turbulence Modelling and Measurements (ETMM-8).* Marseille-France, June 9-11, 2010.

Paper 5. Gallardo, J. P., El Khoury, G. K., Pettersen, B. & Andersson, H. I. 2010 Effects of uniform shear on the flow past a curved circular cylinder. *The* 5^{th} *European Conference on Computational Fluid Dynamics (ECCOMAS).* Lisbon-Portugal, June 14-17, 2010.

Contents

Part 1

Summary

CHAPTER 1

Introduction

Fluid flows comprise a wide variety of complex flow phenomena which depend on the geometrical configuration of the problem as well as on the Reynolds number of the flow (Re). Based on the value of the latter non-dimensional parameter, a fluid motion can be classified as laminar or turbulent. Laminar flows exist at relatively low Reynolds numbers and, in this case, the motion of the fluid particles can be predictable and along observable paths. However, it is well known that most fluid flows observed in nature or encountered in engineering applications are turbulent. This is because many gases and liquids have extremely low viscosity and, therefore, most practical flows are characterized by large values of the Reynolds number.

There is merely no formal definition of turbulence. According to many researchers it is simply better to note that when the inertial forces are large in comparison to viscous forces (low viscosity ν), the flow develops a chaotic random motion and is highly unpredictable. In this case, the flow field is very sensitive to perturbations and fluctuates wildly in time and space. Additionally, it contains swirling flow structures (eddies) with characteristic length, velocity and time scales which are spread over broad ranges. The size of the largest eddies in a turbulent flow is determined by the characteristic length scale of the mean flow whereas for the smallest eddies, their size depends on the Reynolds number. At high Reynolds numbers, there is a wide range of eddy sizes. The largest eddies, which are generated directly by shear in the mean flow, contain most of the turbulent kinetic energy and are unaffected by viscous stresses. However, due to inertial effects these large eddies break-down and transfer energy to smaller eddies that by its turn spread the energy to yet smaller structures. This process continues until a scale is reached at which the inertial forces become comparable to the viscous stresses and the kinetic energy is dissipated by the latter into heat.

1.1. Navier-Stokes equations

The spatial and temporal evolution of a viscous fluid can be described by the Navier-Stokes equations. These equations are derived by applying Newton's second law to a continuum, the principle of mass conservation and a constitutive law which relates the shear stresses in a fluid to the rate of deformation of a fluid element. In the present thesis, we consider a linear stress-strain relation and thus the fluid is Newtonian. Based on these assumptions and by

considering an incompressible isothermal fluid, the Navier-Stokes equations are expressed as:

$$\frac{\partial u_i}{\partial x_i} = 0, \tag{1.1}$$

$$\frac{\partial u_i}{\partial t} + u_j \frac{\partial u_i}{\partial x_j} = -\frac{1}{\rho}\frac{\partial p}{\partial x_i} + \nu \frac{\partial^2 u_i}{\partial x_j x_j}, \quad i = 1, 2, 3 \tag{1.2}$$

Here, ρ and ν are the density and the kinematic viscosity of the fluid, respectively. It is often convenient to work with a non-dimensional form of the Navier-Stokes equations. By introducing representative scales for velocity, length, time and pressure, U, L, L/U and ρU^2 (the velocity and length scales have to be chosen appropriately to the flow problem considered), a non-dimensional form of the Navier-Stokes equations is obtained and a Reynolds number can be defined as:

$$Re = \frac{UL}{\nu} \equiv \frac{inertial forces}{viscous forces} \tag{1.3}$$

The Reynolds number can be interpreted as a measure of the inertial forces divided by the viscous forces, and is by far one of the most important non-dimensional numbers in fluid mechanics.

1.2. Direct numerical simulation

Direct numerical simulation (DNS) is perhaps the most straightforward approach available to numerically solve the Navier-Stokes equations. It involves no turbulence modelling and directly solves the equations of fluid motion capturing all eddies in the flow field ranging from the characteristic length scale (L) right down to the Kolmogorov length scale (η) related to the smallest eddies. The Kolmogorov scales represent the smallest turbulent motions and are defined as:

$$\eta \equiv \left(\frac{\nu^3}{\varepsilon}\right)^{1/4} \tag{1.4}$$

$$\tau_\eta \equiv \left(\frac{\nu}{\varepsilon}\right)^{1/2} \tag{1.5}$$

$$u_\eta \equiv (\nu\varepsilon)^{1/4} \tag{1.6}$$

for length, time and velocity, respectively. Here, ε denotes the turbulent kinetic energy dissipation. By considering an inviscid estimate for the dissipation rate; i.e. $\varepsilon \sim U^3/L$ and the Reynolds number introduced in the previous subsection, the following ratio between the smallest and largest scales is obtained:

$$\frac{\eta}{L} \sim Re^{-3/4} \tag{1.7}$$

It is apparent from the above relation that the separation in scales increases dramatically with the increase in the Reynolds number. In fact, the number of grid points needed to perform a three-dimensional DNS is proportional to $Re^{9/4}$. By taking into consideration the total increase in the number of time steps associated with the increase in Re ($L/U\tau_\eta \sim Re^{1/2}$) , it can be concluded that the computational cost in DNS roughly grows by Re^3. With such high computational costs, DNS is mainly used as a research tool to study moderately low Reynolds number flows.

CHAPTER 2

Inflow conditions

The generation of realistic dynamic inflow conditions for spatially developing turbulent flows is among the most fundamental issues in direct numerical simulations. Accordingly, it is hardly surprising that this problem has attracted considerable interest among researchers since the usage of periodic boundary conditions is severely restricted or not suitable in many practical geometrical configurations. This is because of the flow inhomogeneity in more than one direction. Several methods of different complexity have been previously investigated in order to provide realistic inflow data for inhomogeneous turbulent flows.

In numerical simulations of turbulent boundary layers, Spalart & Watmuff (1993) solved the incompressible Navier-Stokes equations over a flat plate using periodic boundary conditions in the x and z directions parallel to the plate. Although such a flow problem in not homogeneous in the x-direction, the authors made it feasible to use periodic boundary conditions in the latter direction by introducing a fringe region technique. In this method, a forcing term is applied on the Navier-Stokes equations and within a certain period in x they distinguished between a fringe region, close to the inflow and outflow boundaries, in which the added terms are finite and a useful region in which they are zero. Subsequently, the flow profile close to the outflow is returned to the desired inflow profile in the fringe region.

Perhaps one of the most studied flow configurations in which periodic boundary conditions has been employed is the turbulent plane channel flow; see e.g. Kim *et al.* (1987). In this case, the flow is homogeneous in the streamwise and spanwise directions while at the same time exhibits strong inhomogeneity in the wall-normal direction. Nevertheless, there is a vast variety of wall-bounded flows in which the flow is not homogeneous in the streamwise direction, such as sudden expansion channels. This emphasizes the need to develop reliable methods to generate proper inflow conditions for spatially developing wall-bounded flows. One of the traditional and most simple approaches is to impose perturbation on a laminar solution from which the turbulence then develops. However, this may require long computational domains in order that realistic turbulence develops properly from the added perturbations. Nonetheless, other methods have been employed by researches, as for instance, proper orthogonal decomposition (POD).

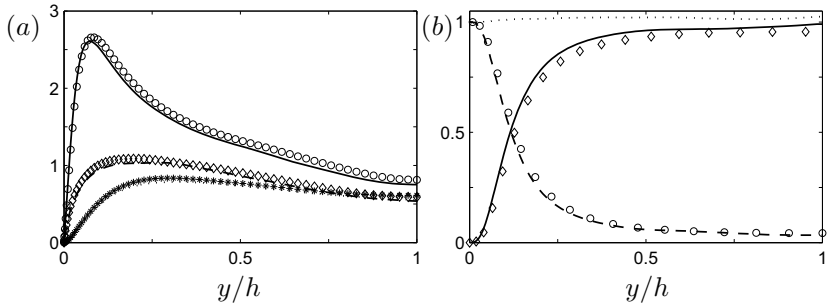

FIGURE 2.1. Cost-effective method applied to inhomogeneous wall-bounded flows. (a) Comparison with DNS data from Kim *et al.* (1987) for fully developed turbulent Poiseuille flow. Turbulent intensities: ———, ∘, streamwise direction; · · · · · · ·, ∗, wall-normal direction; – – – –, ⋄, spanwise direction. (b) Comparison with DNS data from Bech *et al.* (1995) for fully developed turbulent Couette flow. Shear stress variations: – – – –, ∘, viscous shear stress; ———, ⋄, turbulent shear stress; · · · · · · ·, total shear stress τ.

A more realistic approach to generate proper turbulent inflow conditions for spatially developing channel flows would involve the utilization of an auxiliary simulation. In this case, the auxiliary simulation is run with streamwise periodicity and synchronously with the actual computation under consideration. Thereafter, instantaneous velocity fields are taken from the auxiliary simulation and simultaneously fed at an inflow of the main simulation in order to mimic a long channel section upstream the inlet of the spatially developing problem. However, since this method demands the run of two separate simulations simultaneously, it can be very expensive in terms of CPU time. To address this issue, a newly developed technique is introduced to generate dynamic inflow conditions for inhomogeneous turbulent flows; see Barri *et al.* (2009). The method, referred to as the cost-effective method, consists of recycling finite-length time series (ts) of instantaneous velocity profiles at the input of the simulation under consideration. These profiles are taken from a precursor simulation and a physical constraint is introduced on the length of the time series t_s to be of order of the large-eddy-turnover-time. Figure 2.1 displays the turbulence intensities and shear stress variations obtained via the cost-effective method in the inlet section of DNS studies of turbulent channel flow with an obstruction and turbulent Couette flow over a backward-facing step. The agreement between the simulation and the DNS data of Kim *et al.* (1987) and Bech *et al.* (1995) is rather satisfactory which demonstrate the ability of the present technique to generate suitable inflow conditions for inhomogeneous turbulent flows.

CHAPTER 3

Wall-bounded flows

3.1. One-sided expansion channels

Due to its geometrical simplicity, the flow over a backward facing step (BFS) has been extensively investigated through the past few decades in order to study wall-bounded separated flows. Typical prototypes of BFS flows are the boundary layer, the plane channel and the Couette flow cases; see e.g. Eaton & Johnston (1981) and Le *et al.* (1997). A common feature of these flows is the existence of a shear layer emanating from the step corner and reattaching further downstream leading to the formation of a recirculation bubble. The presence of the internal shear layer and the massive recirculation zone gives rise to complex flow dynamics which for instance affect the turbulence production and Reynolds stress anisotropy.

Nevertheless, the most studied BFS flow is the pressure-driven flow in a plane channel with a sudden one-sided expansion; see e.g. Barri *et al.* (2010). Owing to the principle of mass conservation, the Reynolds number remains the same downstream of the step as in the upstream part of the channel. In a BFS Couette flow, on the other hand, the Reynolds number becomes higher downstream of the step. It is well known that the shear-driven turbulent Couette flows (Bech *et al.* 1995) exhibit a number of characteristic features which make them distinguishingly different from the pressure-driven Poiseuille flow, notably the monotonically increasing mean velocity profile.

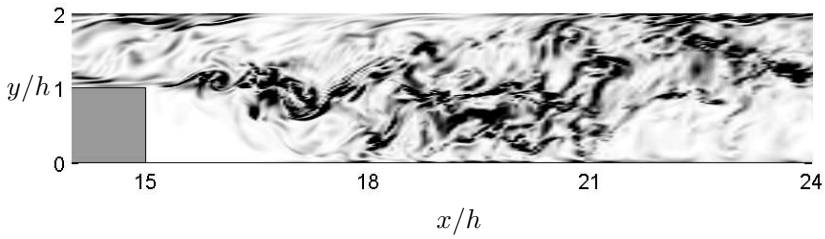

FIGURE 3.1. Instantaneous enstrophy contours revealing the formation of Kelvin-Helmholtz instabilities in turbulent Couette backward-facing step flow.

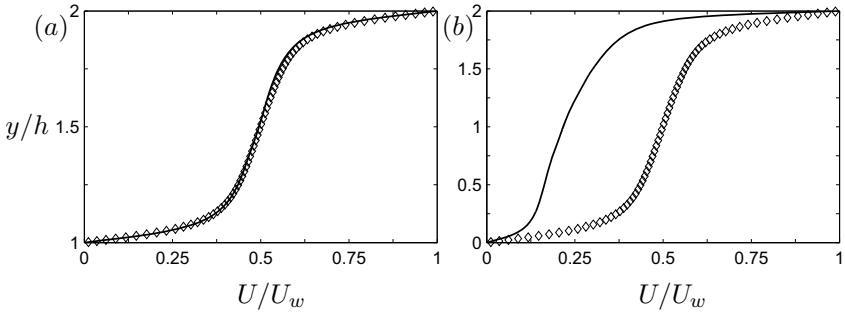

FIGURE 3.2. Mean velocity profile normalized by the upper wall velocity U_w. (a) Inlet section; (b) recovery region. The symbols denote DNS data from Bech *et al.* (1995).

Since the turbulent flow field in BFS Couette flow evolves spatially in the streamwise direction, special attention must be paid to the boundary condition at the input. For this purpose, the cost-effective method introduced in the previous chapter is utilized to generate realistic dynamic inflow conditions from a precursor simulation. Depicted in figure 3.2 is the mean velocity profile at two representative locations: in the upstream channel close to the inlet, and in the recovery region far downstream the step. At the former position, excellent agreement is observed with the DNS data from Bech *et al.* (1995), while at the latter position the profile is yet far from being anti-symmetric. Midway between the walls U is still roughly half of $U_w/2$ which should have been reached in the case of a fully redeveloped Couette flow. Nonetheless, irrespective of the length of the domain that can be used in the downstream part of the channel, an anti-symmetric profile corresponding to a fully redeveloped Couette flow will not be reached. This is due to the principle of mass conservation. It follows that since the height of the domain after the step is twice that of the inlet section and the mean velocity profile of Couette flow is monotonically increasing to a constant value of U_w, the flow cannot adjust itself to an anti-symmetric S-profile shape and at the same time maintain a constant flow rate.

This observed pattern is a distinctive feature in the BFS Couette flow. The two-dimensional upstream mean flow develops to an essentially unidirectional flow in the downstream part of the computational domain, i.e. beyond $x/h \approx 30$ or 15 step heights h downstream of the sudden expansion. It is noteworthy that the upstream pure Couette flow redevelops into a mixed Couette-Poiseuille flow in contrast to the classical pressure-driven backward-facing step flow where an upstream Poiseuille flow inevitably redevelops to another pure Poiseuille flow far downstream of the step. In the present case, however, an adverse pressure gradient is established with the view to assure global mass conservation. The resulting mixed Couette-Poiseuille

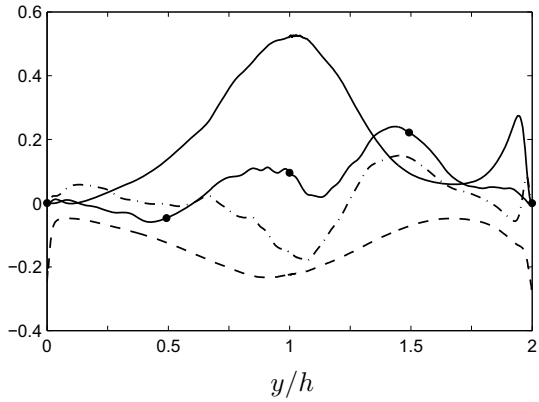

FIGURE 3.3. Turbulent kinetic energy budget normalized by $u_{\tau i}^4/\nu$ at $x/h = 18$. ———, P_K; – – – –, $-\epsilon_K$; — · —, T_K; ——●——, $U_k \partial(q^2/2)/\partial x_k$.

flow exhibits major asymmetries in the turbulence field with a substantially reduced turbulence level along the stationary wall, and closely resembles the Couette-Poiseuille flow simulations reported by Kuroda *et al.* (1995).

In order to study the shear layer which forms when the upstream Couette flow mixes with the recirculating flow downstream of the step, the turbulent kinetic energy budget is presented at a streamwise position passing through the center of the primary separation zone (i.e. $3h$ downstream of the step). The transport equations for the Reynolds stress tensor are:

$$\frac{D}{Dt}(\overline{u_i u_j}) = P_{ij} - \varepsilon_{ij} + \Pi_{ij} + G_{ij} + D_{ij} + T_{ij} \tag{3.1}$$

where the production, dissipation, pressure-strain, pressure diffusion, molecular diffusion and turbulent diffusion are defined as:

$$P_{ij} = -\overline{u_i u_k}\frac{\partial U_j}{\partial x_k} - \overline{u_j u_k}\frac{\partial U_i}{\partial x_k} \tag{3.2}$$

$$\varepsilon_{ij} = 2\nu\overline{\frac{\partial u_i}{\partial x_k}\frac{\partial u_j}{\partial x_k}} \tag{3.3}$$

$$\Pi_{ij} = \frac{1}{\rho}\left(\overline{p\frac{\partial u_i}{\partial x_j} + p\frac{\partial u_j}{\partial x_i}}\right) \tag{3.4}$$

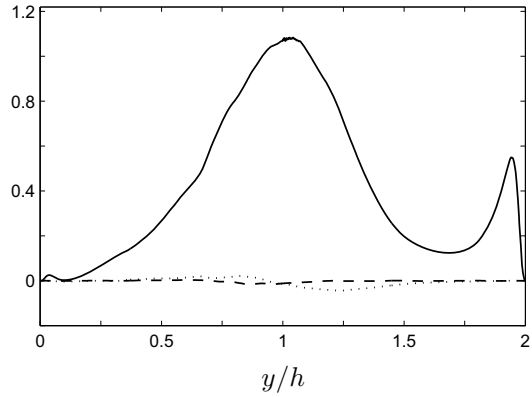

FIGURE 3.4. Turbulent production terms normalized by $u_{\tau i}^4/\nu$ at $x/h = 18$. ———, P_{11}; · · · · · · · , P_{22}; – – – –, P_{33}.

$$G_{ij} = -\frac{1}{\rho}\left(\frac{\partial}{\partial x_i}\overline{pu_j} + \frac{\partial}{\partial x_j}\overline{pu_i}\right) \tag{3.5}$$

$$D_{ij} = \nu\frac{\partial^2}{\partial x_k^2}\overline{u_i u_j} \tag{3.6}$$

$$T_{ij} = -\frac{\partial}{\partial x_k}\overline{u_i u_j u_k} \tag{3.7}$$

The budget for the turbulent kinetic energy $\overline{q^2}/2 = \overline{u_i u_i}/2$ is one half the sum of the budget of the diagonal components of the Reynolds stress tensor, and is shown in figure 3.3. In the shear layer, production and dissipation are the most dominant terms whereas turbulent diffusion transports energy into the upper half part of the channel only. The contribution to P_K comes mainly from P_{11} (see figure 3.4) and its peak at $y/h \approx 1$ is almost 2.5 times larger than that of ϵ_K. This infers that dissipation is not in balance with production.

In the regions close to the wall, turbulence is substantially damped along the lower one due to recirculation. In this case, the production and turbulent diffusion terms are almost negligible which is in contrast to viscous dissipation that is the most significant (among the plotted terms).

Since there is nearly no production of $\overline{v^2}$ and $\overline{w^2}$ as can be inferred from figure 3.4, their only source of energy is from Π_{ij} which serves to redistribute energy between the normal stresses. This is shown in figure 3.5 where the pressure-strain terms appearing in the $\overline{u^2}$, $\overline{v^2}$ and $\overline{w^2}$ equations are plotted together at $x/h = 18$. Across the channel, $\overline{ww}$ acts as a receiving component taking energy mainly from $\overline{uu}$. The profiles of Π_{11} and Π_{22}

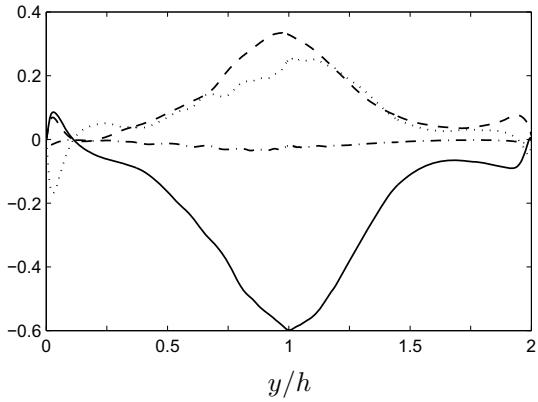

FIGURE 3.5. Pressure-strain terms normalized by $u_{\tau i}^4/\nu$ at $x/h = 18$. ———, Π_{11}; · · · · · · · , Π_{22}; – – – –, Π_{33}; — · —, Π_{ii}.

indicate a qualitative difference in the energy exchange pattern between the two walls. While there is a large energy transfer from the $\overline{vv}$ component to the $\overline{uu}$ and $\overline{ww}$ between $y/h = 0$ and $y/h \approx 0.2$, $\overline{uu}$ contributes to $\overline{vv}$ in delivering energy to $\overline{ww}$ in the region near to the upper wall. Away from the walls, the major effect of the pressure-strain is to distribute energy from $\overline{uu}$ component to the other two components. The sum of the three components (i.e. Π_{ii}) is almost zero and this supports the adequacy of the sampling procedure.

3.2. Plane channel with an obstruction

Asymmetric flow patterns that develop in symmetric channel configurations are of considerable interest in a variety of industrial applications. Turbulent mixing and the rate of heat transfer are for instance among the physical mechanisms affected by flow asymmetry. Perhaps the most studied geometrical configuration related to such flows is the flow in a plane channel with a double-sided symmetric expansion; see e.g. Durst *et al.* (1974). A somewhat related problem is a plane channel configuration with a single or a sequence of thin-plate obstructions. In a similar approach to the previous study, the cost-effective method is used to provide realistic fully turbulent inflow conditions in order to study the asymmetric flow pattern caused by a single thin-plate obstruction in a plane channel. In this case, however, the precursor simulation is that of a fully-developed turbulent channel flow. The resulting flow field upstream the obstruction compares almost perfectly well with data from Kim *et al.* (1987). It is worthwhile to note that the

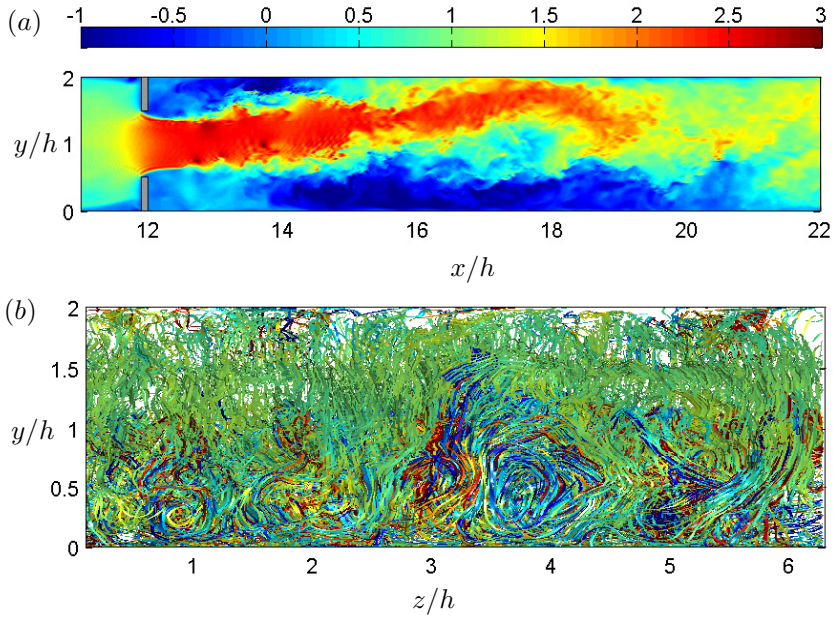

FIGURE 3.6. Asymmetric flow pattern in a symmetric channel configuration with a single thin-plate obstruction. (a) Side view showing the instantaneous streamwise velocity u normalized by bulk velocity at the input U_i. (b) Upstream view from $x/h = 20$ in terms of velocity stream ribbons.

current DNS study focuses on the asymmetric flow pattern in the fully developed turbulent state and not on the source of or mechanism for creating the asymmetry phenomenon.

In the present findings, the flow downstream the obstruction is asymmetric with an extraordinarily long separation bubble at one of the walls. This separation bubble extends about 17 obstruction heights downstream of the thin-plate, and is almost 4 times longer than the shorter bubble found on the other wall. After the distinctly asymmetric pattern has been established as in figure 3.6(a), the jet remains deflected to the same side due to the substantially lower pressure within the shorter recirculating eddy. A previous DNS study on a similar problem was carried out by Makino *et al.* (2008) but with a periodically repeating obstruction at a slightly lower Reynolds number. For that purpose, the authors used periodic boundary conditions in the streamwise direction. In comparison with their findings, the longest of the two bubbles found in the present case exceeds the downstream length

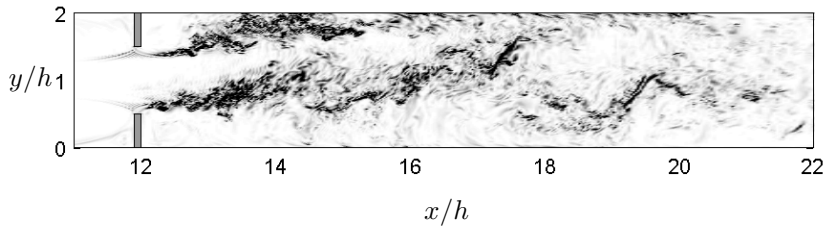

FIGURE 3.7. Instantaneous enstrophy in a side view plane.

of the domain used by Makino *et al.* (2008). This verifies the necessity of proper inflow conditions if the effects of a single obstruction is to be studied.

An insight on the complex motion in the present study is obtained from figure 3.6(b) where stream ribbons of the instantaneous velocity components are shown in an upstream perspective view from $x/h = 20$. Stream ribbons illustrate the direction of the flow and are constructed as narrow surfaces defined between two adjacent streamlines. Large-scale motions are observed in the lower-half of the channel which is in contrast to the upper-half where the flow is relatively calm. These swirling motions transport fluid between the primary recirculation region on the lower wall and the high-speed jet and simultaneously influence the Reynolds stresses. Meanwhile, the formation of Kelvin-Helmholtz vortices is visible from figure 3.7. They are generated around the top edges of the slits and swept away forming a fine-scale turbulence in the mixing layers. The absence of vorticity between the two mixing layers indicates a potential-like type flow (i.e. irrotational flow) in this region which is due to flow acceleration.

In a quick look at the momentum balance, the streamwise momentum equation for a channel flow with single thin-plate obstruction can be written as:

$$U\frac{\partial U}{\partial x} + V\frac{\partial U}{\partial y} = -\frac{1}{\rho}\frac{\partial P}{\partial x} - \frac{\partial}{\partial x}\left(\overline{uu}\right) - \frac{\partial}{\partial y}\left(\overline{uv}\right) + \nu\left(\frac{\partial^2 U}{\partial x^2} + \frac{\partial^2 U}{\partial y^2}\right) \quad (3.8)$$

Here, the left hand side of equation 3.8 denotes the convective accelerations, and the term with $\partial/\partial t$ is ignored since the flow is considered to be statistically steady. The above equation can be rearranged as follows:

$$0 = -\frac{1}{\rho}\frac{\partial P}{\partial x} + \frac{\partial}{\partial x}\left(\nu\frac{\partial U}{\partial x} - \overline{uu} - U^2\right) + \frac{\partial}{\partial y}\left(\nu\frac{\partial U}{\partial y} - \overline{uv} - UV\right) \quad (3.9)$$

In the present case, $-UV$ is a result of the effect of the slits on the mean flow field as shown in figure 3.8(a). As the flow contracts, U is positive whereas V attains positive and negative values in the lower and upper parts

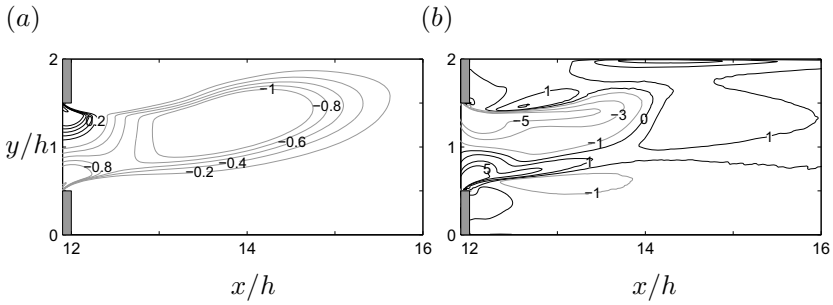

FIGURE 3.8. (a) Contours of the product $-UV/U_i^2$. (b) Contours of wall-normal pressure gradient $\partial P/\partial y$.

of the channel, respectively. Downstream the constriction, the sign of V depends on the direction in which the flow bends. Since the flow bends upwards in the present case, the positive values of U and V give a negative $-UV$. In figure 3.8(b), the pressure gradient $\partial P/\partial y$ attains substantial negative values in the mixing layer downstream of the upper slit, i.e. P is lower in the recirculation zone than in the jet flow. The upward pressure force $-\partial P/\partial y$ therefore tends to bend the mixing layer towards the upper wall.

CHAPTER 4

Bluff body flows

4.1. Flow past a prolate spheroid

A wake develops behind a bluff body if the Reynolds number exceeds a certain critical value such that the flow separates from the surface of the body. The resulting wake flow may be steady or unsteady and even become turbulent depending on the actual value of the Reynolds number Re. The shape of the body itself, as well as its orientation relative to the oncoming flow, determines the symmetry of the resulting wake. The two most frequently studied bluff bodies are the sphere and the circular cylinder (see e.g. Johnson & Patel 1999 and Zdravkovich 1997) which at fairly low Reynolds numbers give rise to axisymmetric and planar wakes, respectively.

A prolate spheroid is a three-dimensional body with two different length scales, one plane of symmetry, and one axis of symmetry. The ratio between the semi-major and semi-minor axes, i.e. the aspect ratio, is a measure of departure from a spherical body. Spheroids with aspect ratios 8:1, 6:1, and

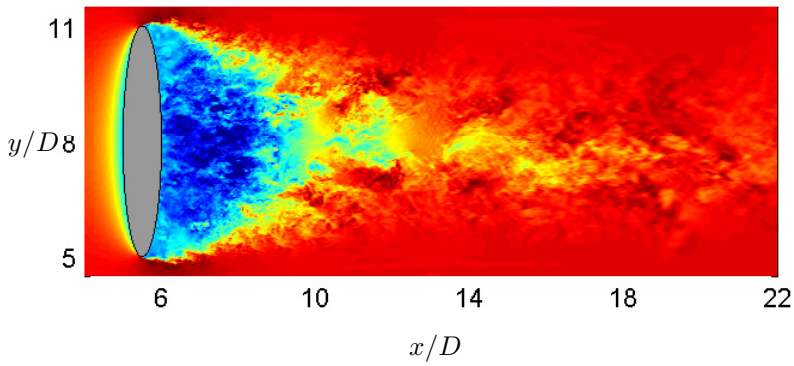

FIGURE 4.1. Crossflow past a 6:1 a prolate spheroid. The figures represents the instantaneous streamwise velocity u/U_o in the meridional plane at $Re = 10\,000$. Here, the colors vary from -0.5 (dark blue) to 1.2 (dark red) while light green represents 0.

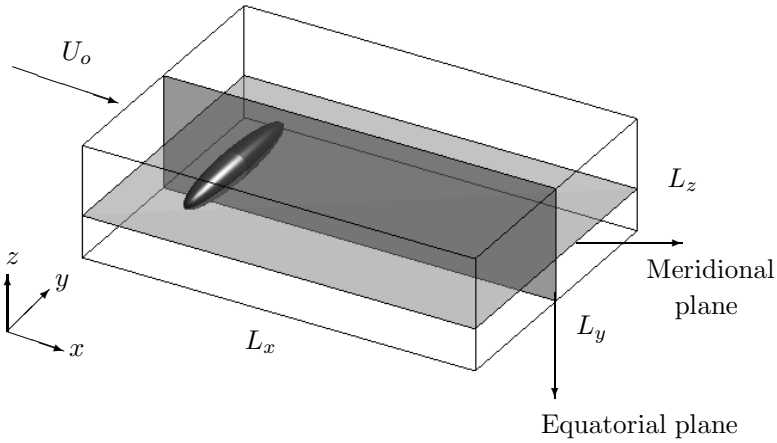

FIGURE 4.2. Schematic view of flow over a 6:1 prolate spheroid at high incidence. The major axis is taken to be perpendicular, i.e. at 90°, to the main flow direction. With this orientation the spheroid plays the role of a bluff body rather than a slender object.

3:1 can be considered as simplified models of submarines, unmanned underwater vehicles, missiles, airships, etc. When the aspect ratio is relatively high and the major axis is aligned with the flow the prolate spheroid behaves as a slender body. If, on the other hand, the inflow is perpendicular to the symmetry axis, i.e. parallel with the equatorial plane, the spheroid plays the role of a bluff body and the wake can be expected to possess two mutually perpendicular symmetry planes. The wake behind this spheroid shares some features of the cylinder wake and others of the wake of a sphere.

The wake behind a prolate spheroid without incidence is axisymmetric, at least at low Re, just as is the wake of a sphere. The axisymmetry is broken by the incidence angle and in the particular case of 90° angle of attack it can be anticipated that the wake at mid-span will resemble the wake behind circular cylinders. In the Reynolds number range up to 300, Sheard *et al.* (2008) reported that the vortices shed in the vicinity of the cylinder mid-span resembled Kármán vortices when the length-to-diameter ratio exceeded 4. The helical-like wake which may occur behind a sphere at higher Re due to the shedding of hairpin vortices at varying azimuthal locations will probably be prohibited in a wake behind a prolate spheroid in crossflow provided that the aspect ratio is sufficiently above 1.

At fairly low Reynolds numbers, a toroidal vortex ring develops on the rear side of a sphere; see for instance Achenbach (1974) and Johnson & Patel (1999). In the present case, however, the elliptical rather than circular

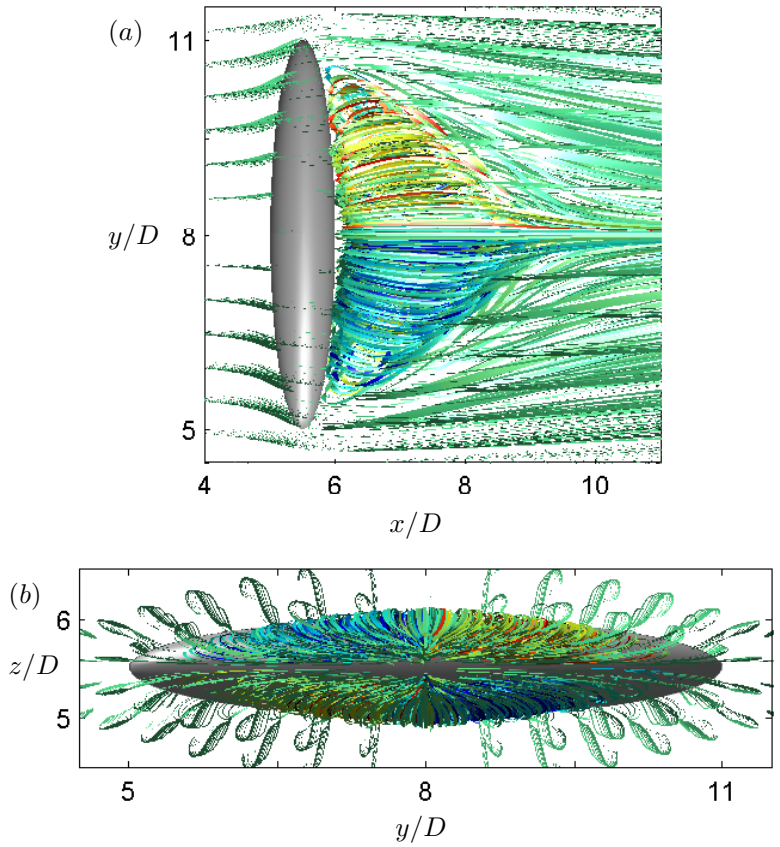

FIGURE 4.3. Steady flow past a prolate spheroid at $Re = 50$ visualized by means of velocity stream ribbons. (a) Top view; (b) upstream view from $x/D = 10$.

cross-section of the spheroid severely breaks the axisymmetry of the vortex ring and leaves the stretched vortex structure shown in figure 4.3(a). The 'croissant'-like shape results from the recirculating flow above the meridional plane $z/D = 5.5$, while a mirror-shaped vortex structure is present below the meridional plane. Due to the prevailing flow symmetries at $Re = 50$, no exchange of fluid between the two halves take place. The upstream view into the wake from the cross-sectional (y, z)-plane, $4.5D$ downstream of the major axis of the spheroid in figure 4.3(b), gives another impression of the three-dimensional wake topology. The shape of the stream ribbons becomes gradually more distorted with the distance from mid-span and a stream ribbon emerging from the polar area is almost parallel with the meridional (x, y)-plane.

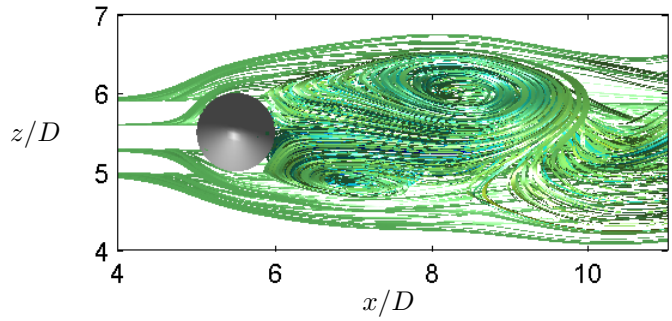

FIGURE 4.4. Side view showing the instantaneous flow configuration at $Re = 100$ in terms of velocity stream ribbons.

The complexity of the flow topology increases with Re and the asymmetry about the meridional plane is evident even for $Re = 100$ in figure 4.4 where a closed recirculation bubble does no longer exist as in the steady case. The upper vortical structure in figure 4.4 is considerably larger than the oppositely rotating lower vortex. The fluid which is deflected upwards as the spheroid is approach seems to follow the contours of the upper vortex. A part of this fluid is entrained into the spiraling vortex whereas another part proceeds in the upstream direction and eventually feeds the lower vortex. The oncoming fluid which is deflected downwards, however, is directly fed into the counter-clockwise vortex.

The frontal area of the prolate spheroid in crossflow is elliptical. At least in the far wake, one may expect that the flow would resemble the wake formed behind sharp-edged elliptical disks. The plot of u/U_o in the meridional plane in figure 4.1 gives the impression that the wake contracts to a narrow band in the spanwise direction as the flow progresses downstream. A clearer view of this phenomenon can be seen from the cross-stream slices depicted in figure 4.5. It is readily observed that the axis of the wake has switched at $x = 20D$, in the sense that the major axis of the wake now is aligned with the minor axis of the spheroid for the Reynolds numbers under consideration here. Moreover, the shape of the near-wake reflected the elliptical shape of the meridional cross-section of the spheroid. Some $10D$ downstream, however, the major axis of the wake became aligned with the minor axis of the spheroid. A similar axis switching was observed experimentally by Kuo & Baldwin (1967) and Kiya & Abe (1999) in the wake behind an elliptical disk. In that case, the authors reported that axis switching occurred at about $4D$ downstream of the disk, i.e. significantly closer to the bluff body than in the present study. While Kuo & Baldwin (1967) avoided to present a hypothesis on the reason why the wake grow non-uniformly behind elliptical bluff

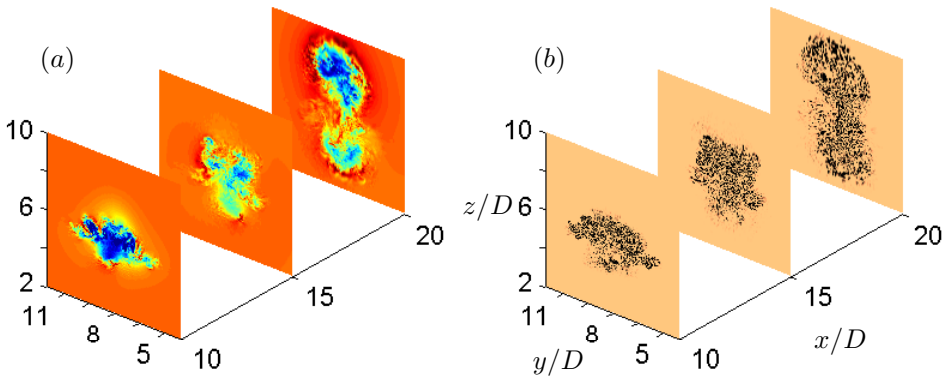

FIGURE 4.5. Cross-stream slices at $Re = 10\,000$. (a) Instantaneous streamwise velocity u/U_o where the colors vary from 0.4 (dark blue) to 1.2 (dark red); (b) $-\lambda_2$ via the method of Jeong & Hussain (1995).

bodies, Kiya & Abe (1999) attributed the mechanism of axis switching to different growth rates of the wake in the plane of the major and minor axis.

CHAPTER 5

Review of papers content

In this chapter, a brief summary of each of the five articles included in part two of the thesis is presented. The first three papers address wall-bounded flows while the last two are concerned with uniform flow past prolate spheroid at incidence.

Paper 1: **Inflow conditions for inhomogeneous turbulent flows.**
Barri, M., El Khoury, G. K., Andersson, H. I. & Pettersen, B.

In this paper, a new technique, referred to as the cost-effective method, is introduced in order to generate realistic dynamic inflow conditions for spatially developing wall-bounded turbulent flows. This method consists of recycling finite-length time series (ts) of instantaneous velocity profiles at the input of the simulation under consideration. The profiles are taken from a precursor simulation and a physical constraint is introduced on the length of the time series t_s to be of order of the large-eddy-turnover-time. Excellent agreement with fully developed channel flow statistics is observed when t_s equals or exceeds the large-eddy-turnover-time time scale. The present results are more realistic than those obtained with synthetic turbulence generation and at the same time substantially cheaper than running an auxiliary simulation in parallel.

Paper 2: **Massive separation of turbulent Couette flow in a one-sided expansion channel.**
El Khoury, G. K., Andersson, H. I., Barri, M. & Pettersen, B.

The newly developed technique presented in the preceding paper is used here in order to study the wall-driven flow over a backward-facing step by means of direct numerical simulation. In this case, the precursor simulation was that of plane Couette flow at exactly the same Reynolds number as in the extensive investigation by Bech *et al.* (1995). An interesting feature in the present study is that the mean streamwise velocity U does not retain the characteristic S-shape typical of a pure Couette flow far downstream the step. This phenomenon is ascribed to the principle of global mass conservation, which can be fulfilled only if an adverse mean pressure gradient is established in the recovery region. This is indeed what is observed in the recovery region where a Couette-Poiseuille flow type prevails.

Paper 3: **Asymmetries in an obstructed turbulent channel flow.**
El Khoury, G. K., Pettersen, B., Andersson, H. I. & Barri, M.

This paper concerns the asymmetric flow pattern that develops in a symmetric channel configuration with a single thin-plate obstruction. In a similar approach to paper two, the cost-effective method is used to provide realistic fully turbulent inflow conditions from a precursor simulation. In the present study, however, the precursor simulation is that of a fully-developed turbulent channel flow. A previous DNS study on a similar problem was carried out by Makino *et al.* (2008) but with a periodically repeating obstruction at a slightly lower Reynolds number. For that purpose, the authors used periodic boundary conditions in the streamwise direction. In comparison with their findings, the longest of the two bubbles found in the present case exceeds the downstream length of the domain used by Makino *et al.* (2008). This verifies the necessity of proper inflow-outflow conditions if the effects of a single obstruction is to be studied.

Paper 4: **Wakes behind a prolate spheroid in crossflow.**
El Khoury, G. K., Andersson, H. I. & Pettersen, B.

In this paper, the flow of a viscous fluid past a prolate spheroid has been investigated numerically at some different Reynolds numbers in the laminar flow regime. Contrary to earlier investigations, the major axis of the spheroid was oriented perpendicular to the oncoming flow. The wake flow therefore showed some similarities with the wake behind finite-length circular cylinders and yet also resembled the axi-symmetric wake behind a sphere in some other aspects. The wake behind the 6:1 spheroid remained steady at the lowest Reynolds numbers considered, $Re = 50$ and 75. An unsteady wake was observed at $Re = 100$, although the flow field still retained its symmetry about the equatorial plane. A symmetry-breaking occurred at a somewhat higher Reynolds number and more complex wake patterns were seen at $Re = 200$ and 300. Double-sided hairpin vortices, shed alternately from the two sides of the spheroid, were essential ingredients of the periodic flow field at $Re \geq 100$. The contours of the nonaxisymmetric near-wake mimicked the shape of the spheroid. Following a switching of the axes of the wake some 10 minor diameters downstream, the major axis of the wake became aligned with the minor axis of the spheroid.

Paper 5: **Crossflow past a prolate spheroid at Reynolds number of 10 000.**
El Khoury, G. K., Andersson, H. I. & Pettersen, B.

This paper represents a continuation of the previous work presented in paper 4 on crossflow past a 6:1 prolate spheroid. While the low Reynolds numbers effects are investigated in the previous paper, the current DNS simulation

focuses solely on the subcritical Reynolds number of 10 000. At this Reynolds number, the boundary layer separated from the frontal side of the spheroid was also found to be laminar and formed an elliptical vortex sheet. In this case, however, the detached shear layer was unstable from its very inception and even the near-wake turned out to be turbulent. The Strouhal number associated with the large-scale shedding was 0.156, significantly below that of the wake of a sphere. A higher-frequency mode was associated with Kelvin-Helmholtz instabilities in the detached shear layer. The shape of the near-wake mirrored the shape of the spheroid. Some 10 minor diameters downstream, the major axis of the wake became aligned with the minor axis of the spheroid.

Acknowledgment

First of all, I would like to thank Professor Helge I. Andersson for his support, encouragement and inspiration throughout the past four years. This work would have not been possible without his continuous guidance and suggestions.

I am also grateful to Professor Bjørnar Pettersen for his help during my PhD work. Furthermore, I would like to acknowledge my friend and colleague Musfata Barri from the department of energy and process engineering at NTNU for the mutual collaboration we had together during the past few years.

My time in Trondheim was made enjoyable in large part due to my friends and the pleasant work environment at NTNU. For this purpose, I would like to thank my fellow colleagues and the staff at the department of marine technology for providing a pleasant and efficient work environment. I am also grateful to my friends in Trondheim and the time spent with them.

Finally, I would like to express my deepest gratitude to my parents Kamal and Najwa, my brother Elie and his wife Abeer, and to my sister Eleine.

Bibliography

Achenbach, E. 1974 Vortex shedding from spheres. *J. Fluid Mech.* **62**, 209–221.

Barri, M., El Khoury, G. K., Andersson, H. I. & Pettersen, B. 2009 Inflow conditions for inhomogeneous turbulent flows. *Int. J. Numer. Meth. Fluids* **60**, 227–235.

Barri, M., El Khoury, G. K., Andersson, H. I. & Pettersen, B. 2010 DNS of backward-facing step flow with fully turbulent inflow. *Int. J. Numer. Meth. Fluids* **64**, 777–792.

Bech, K. H., Tillmark, N, Alfredsson, P. H. & Andersson, H. I. 1995 An investigation of turbulent plane Couette flow at low Reynolds numbers. *J. Fluid Mech.* **286**, 291–325.

Durst, F., Melling, A. & Whitelaw, J. H. 1974 Low Reynolds number flow over a plane symmetrical sudden expansion. *J. Fluid Mech.* **64**, 111–128.

Eaton, J. K. & Johnston, J. P. 1981 A review of research on subsonic turbulent flow reattachment. *AIAA J.* **19**, 1093–1100.

Jeong, J. & Hussain, F. 1995 On the identification of a vortex. *J. Fluid Mech.* **285**, 69–94.

Johnson, T. A. & Patel, V. C. 1999 Flow past a sphere up to a Reynolds number of 300. *J. Fluid Mech.* **378**, 19–70.

Kim, J., Moin, P. & Moser, R. 1987 Turbulence statistics in fully developed channel flow at low Reynolds number. *J. Fluid Mech.* **177**, 133–166.

Kiya, M. & Abe, Y. 1999 Turbulent elliptic wakes. *J. Fluids Struct.* **13**, 1041–1067.

Kuo, Y. H. & Baldwin, L. V. 1967 The formation of elliptical wakes. *J. Fluid Mech.* **27**, 353–360.

Kuroda, A., Kasagi, N. & Hirata, M. 1995 Direct numerical simulation of turbulent plane Couette-Poiseuille flows: effect of mean shear rate on the near-wall turbulence structures. *Turbulent Shear Flows 9, Springer-Verlag, Berlin* 240–257.

Le, H., Moin, P. & Kim, J. 1997 Direct numerical simulation of turbulent flow over a backward-facing step. *J. Fluid Mech.* **330**, 349–374.

Makino, S., Iwamoto, K. & Kawamura, H. 2008 Turbulent structures and statistics in turbulent channel flow with two-dimensional slits. *Int. J. Heat Fluid Flow* **29**, 602–611.

Sheard, G. J., Thompson, M. C. & Hourigan, K. 2008 Flow normal to a short cylinder with hemispherical ends. *Phys. Fluids* **20**, 041701.

Spalart, P. R. & Watmuff, J. H. 1993 Experimental and numerical study of a turbulent boundary layer with pressure gradients. *J. Fluid Mech.* **249**, 337–371.

Zdravkovich, M. M. 1997 *Flow Around Circular Cylinders.* Oxford University Press.

Part 2

Papers

Part 2.1

Wall-bounded flows

Paper 1

Inflow conditions for inhomogeneous turbulent flows

Barri, M., El Khoury, G. K., Andersson, H. I. & Pettersen, B.

International Journal for Numerical Methods in Fluids **60**, 227–235, 2009.

Is not included due to copyright

Paper 2

Massive separation of turbulent Couette flow in a one-sided expansion channel

El Khoury, G. K., Andersson, H. I., Barri, M. & Pettersen, B.

International Journal of Heat and Fluid Flow **31**, 274–283, 2010.

Included in a special issue of selected papers from *The* 6^{th} *International Symposium on Turbulence and Shear Flow Phenomena (TSFP-6).* Seoul-Korea, June 22-24, 2009.

International Journal of Heat and Fluid Flow 31 (2010) 274–283

Contents lists available at ScienceDirect

International Journal of Heat and Fluid Flow

journal homepage: www.elsevier.com/locate/ijhff

Massive separation of turbulent Couette flow in a one-sided expansion channel

George K. El Khoury [a], Helge I. Andersson [b], Mustafa Barri [b], Bjørnar Pettersen [a,*]

[a] Department of Marine Technology, The Norwegian University of Science and Technology, Trondheim NO-7491, Norway
[b] Department of Energy and Process Engineering, The Norwegian University of Science and Technology, Trondheim NO-7491, Norway

ARTICLE INFO

Article history:
Received 1 September 2009
Received in revised form 20 January 2010
Accepted 23 January 2010
Available online 23 February 2010

Keywords:
Couette flow
Separation
DNS
Backward-facing step

ABSTRACT

Direct numerical simulation has been performed to study wall-driven flow over a backward-facing step at Reynolds number $Re = 5200$ based on the step height h and the upper-wall velocity U_w. The flow configuration consisted of a step with height equal to that of the upstream channel yielding an expansion ratio 2:1. Instantaneous enstrophy contours revealed the formation of Kelvin–Helmholtz instabilities downstream of the step. Intense velocity and vorticity fluctuations were generated in the shear-layer formed between the bulk flow and the massive recirculation zone in the lee of the step. Extraordinarily high turbulence levels persisted in the center region even $7.5h$ downstream of the step, i.e. where the separated shear-layer reattached to the wall. A fully redeveloped Couette flow cannot be reached in the downstream part of the channel due to the principle of mass conservation. The local wall pressure coefficient gave evidence of an adverse pressure gradient in the recovery region, where a Couette–Poiseuille flow type prevailed.

1. Introduction

Turbulent flow over a backward-facing step (BFS) is a simplified case of the general family of separated flows with widespread industrial applications. Although its geometry is simple, the flow physics is still complex. Typical prototypes of BFS flows are the boundary layer, the plane channel and the Couette flow cases, see e.g. Eaton and Johnston (1981). A common feature of these flows is the existence of a shear-layer emanating from the step corner and reattaching further downstream leading to the formation of a recirculation bubble. The presence of the internal shear-layer and the massive recirculation zone gives rise to complex flow dynamics which for instance affect the turbulence production and Reynolds stress anisotropy.

The understanding of the flow over a backward-facing step was initially acquired by experiments and two-dimensional numerical simulations. The early studies were performed by Abbot and Kline (1962) and Goldstein et al. (1970). This type of flow is characterized by the channel expansion ratio *ER* and the upstream Reynolds number. Armaly et al. (1983) conducted experiments on air flow over a backward-facing step with an expansion ratio of 2:1 and provided information on the relationship between the Reynolds number and the reattachment length X_R. The authors covered a wide range of Reynolds numbers from about 50 to 6000 and found that X_R tends to increase with the increase of *Re* in the laminar flow regime and decrease in the transitional one while X_R remains relatively constant in the fully-developed turbulent state. The findings of Kuehn (1980), Durst and Tropea (1981), Ötügen (1991), and Ra and Chang (1990), on the other hand, showed that the reattachment length increases with the expansion ratio.

Owing to the rapid developments in high-performance computing, three-dimensional numerical simulations of turbulent flow over a backward-facing step have been performed since the late 1980s. Friedrich and Arnal (1990) studied high Reynolds number turbulent backward-facing step flow using the large-eddy simulation (LES) technique. This technique was also used by Neto et al. (1993) who performed a numerical investigation of the coherent vortices in turbulence behind a backward-facing step. Later, Le et al. (1997) provided an extensive DNS study of turbulent boundary layer flow over a backward-facing step with an expansion ratio of 6:5 and reported a reattachment length equal to six step heights.

Since the BFS problem is not homogeneous in the streamwise direction, proper inflow conditions are to be employed in order to provide a realistic fully turbulent flow at the input. Several methods of different complexity have been used by researchers in the past years to generate suitable inflow conditions. In the boundary layer backward-facing step flow, Le et al. (1997) imposed a mean velocity profile for a flat plate turbulent boundary at the input (Spalart, 1988), whereas Meri and Wengle (2002) utilized a time-dependent inflow condition from a precursor Poiseuille flow simulation to perform DNS and LES of pressure-driven backward-facing step flow. A recent DNS study on the same flow problem was performed by Barri et al. (2010), where the authors used a cost-effective method to generate realistic dynamic inflow conditions. This technique was proposed by the same authors in an

* Corresponding author. Tel.: +47 735 95533.
E-mail address: bjornar.pettersen@ntnu.no (B. Pettersen).

0142-727X/$ - see front matter © 2010 Elsevier Inc. All rights reserved.
doi:10.1016/j.ijheatfluidflow.2010.01.008

earlier study on numerical simulation of plane channel flow (see Barri et al., 2009) and consists of recycling finite-length time series (t_s) of instantaneous velocity planes at the input. These profiles were taken from a precursor simulation and a physical constraint was introduced on t_s to be of order of the large-eddy-turnover-time. The authors kept the inflow time series discontinuous and showed that this discontinuity in the inflow signal vanishes due to the nonlinear interactions of the turbulent flow.

Due to the principle of mass conservation, the Reynolds number in pressure-driven plane channel flow with a sudden one-sided expansion remains the same downstream of the step as in the upstream part of the channel. In a BFS Couette flow, on the other hand, the Reynolds number becomes higher downstream of the step. It is well known that the shear-driven turbulent Couette flows (see e.g. Bech et al., 1995) exhibit a number of characteristic features which make them distinguishingly different from the pressure-driven Poiseuille flow, notably the monotonically increasing mean velocity profile. The only investigation of BFS Couette flow we are aware of is the recent experimental study by Morinishi (2007). He considered a configuration with the step height h equal to half of the upstream channel height, i.e. with an expansion ratio 3:2. The Reynolds number based on the wall-friction velocity at the input was fixed to 300. This configuration (i.e. fixed ER and $Re_{\tau i}$) allowed the author to investigate the effect of the non-dimensional upstream pressure gradient β_o. By varying β_o Morinishi (2007) set up conditions for the following fully-developed upstream flows: the pure Poiseuille flow, the mixed Couette–Poiseuille flow and the pure Couette flow. For the three cases, the reattachment lengths were almost identical and about $6.5h$ and $2h$ for the primary and secondary recirculation regions, respectively.

In the present study we perform direct numerical simulation (DNS) of turbulent Couette flow over a BFS. This will enable us to gather accurate mean flow and turbulence statistics throughout the flow domain, as well as to explore in detail the instantaneous vortex topology in the shear-layer and the recirculation bubble as well as in the re-development zone. We intentionally considered a BFS configuration, where the flow upstream of the step is the same as that studied by Bech et al. (1995), i.e. a fully-developed turbulent Couette flow.

2. Flow configuration and governing equations

Fig. 1 shows a schematic view of the Couette backward-facing step flow which is composed of a step of height h and an upper-wall moving with velocity U_w. Of particular relevance in backward-facing step flows is the expansion ratio ER. This dimensionless parameter is defined as the ratio between the downstream and upstream channel heights, i.e. $ER = H/(H-h)$. In the present study we consider a flow configuration, where the step height is equal to that of the upstream channel, i.e. $H = 2h$. This gives an expansion ratio of 2:1.

The governing equations are the time-dependent, incompressible Navier–Stokes equations for a viscous fluid expressed in non-dimensional form:

$$\nabla \cdot \mathbf{u} = 0, \tag{1}$$

$$\frac{\partial \mathbf{u}}{\partial t} + (\mathbf{u}\cdot\nabla)\mathbf{u} = -\nabla p + \frac{1}{Re}\nabla^2\mathbf{u}. \tag{2}$$

Here, the variables have been non-dimensionalized by h and U_w and the Reynolds number based on the step height and upper-wall velocity, $Re = U_w h/\nu$, is 5200.

3. Numerical approach

The computational domain has a length of $L_x = 39h$ in the streamwise x-direction including an inlet section $L_s = 15h$, $H = 2h$ in the wall-normal y-direction, and $L_z = 9.43h$ in the spanwise z-direction. A total of $(672 \times 384 \times 192)$ grid points are used in x, y and z, respectively. In order to adequately resolve the turbulence scales in the separation region and the vicinity of the walls, a non-uniform mesh distribution is used in the streamwise and wall-normal directions. Thus for a viscous length scale of $l_i = \nu/u_{\tau i}$, based on the wall-friction velocity at the input $u_{\tau i} = 0.032U_w$, the first grid point next to the walls is at $y^+ \approx 0.083$ while the largest grid spacing is about $\Delta y^+ \approx 2.4$ (measured in wall units). For the streamwise direction, the minimum grid spacing $\Delta x^+ \approx 4.8$ is at the step corner and maximum at the beginning and the end of the domain with $\Delta x^+ \approx 14.8$. A uniform mesh is used in the spanwise z-direction with $\Delta z^+ \approx 8.2$. The grid specification in the inlet section is given in Table 1 together with that of Bech et al. (1995).

No-slip boundary conditions are imposed on the solid surfaces in the domain. The flow in the spanwise direction is assumed to be statistically homogeneous and periodic boundary conditions are imposed. A realistic fully turbulent flow is generated at the input by recycling finite-length time series of the instantaneous velocity planes. This technique was first used by Barri et al. (2009) in a numerical simulation of plane channel flow. The length of the time series for the current simulation was $33h/U_w$. This is consistent with the recommendation of Barri et al. (2009). For a plane Poiseuille flow, they demonstrated that the potential periodicity introduced by the recycling of a finite-length time series vanished when the duration of the time series equaled the large-eddy-turnover-time h/u_τ. The imposition of dynamic Dirichlet conditions at the inflow implies that the flow rate is fixed to that of the precursor simulation. The latter was that of plane Couette flow at exactly the same Reynolds number as in the extensive investigation by Bech et al. (1995). As an outflow condition, we solve the convective equation $\partial\mathbf{u}/\partial t + U_c\partial\mathbf{u}/\partial x = 0$ at the exit plane and set the total normal stress acting on it to zero by means of a pressure boundary condition $-p + 2\mu\partial u/\partial x = 0$. The convective boundary condition was used in previous numerical simulations by Lowery and Reynolds (1986) for a mixing-layer and Le et al. (1997) and Barri et al. (2010) for turbulent flow over a backward-facing step and is considered suitable for vortical structures moving out of the domain.

The DNS code used to numerically solve the governing Eqs. (1) and (2) is MGLET (see Manhart, 2004). MGLET is a finite-volume code in which the Navier–Stokes equations are discretized on a

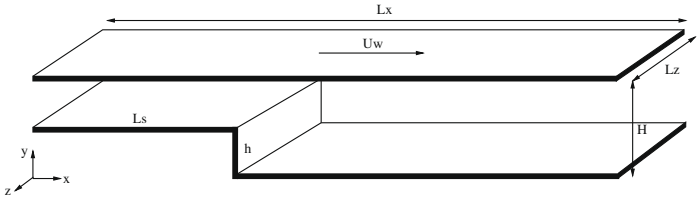

Fig. 1. Flow configuration and coordinate system (not to scale).

Table 1
Computational parameters at the inlet section and in the corresponding reference case (Bech et al., 1995). (The symbol $*$ denotes a division by the channel height in the inlet section $(H-h)$.)

	L_x^*	L_z^*	Δx^+	Δy^+	Δz^+
Bech	5π	2π	10.1	$(0.7, 3.9)$	4
Inlet	4.8π	3π	$(4.8, 14.8)$	$(0.083, 2.4)$	8.2

staggered Cartesian mesh with non-equidistant grid spacing. The discretization is second-order accurate in space. A second-order explicit Adams–Bashforth scheme is used for the time integration. The Poisson equation for the pressure is solved using a multi-grid algorithm.

The simulations were started from an arbitrary flow field and thereafter let to evolve to a statistically steady state. The time step used was $\Delta t = 0.001h/U_w$. Statistics were gathered for $396h/U_w$ after the flow field first had evolved into a statistically steady state.

Direct numerical simulation of turbulent plane Couette flow has been performed in several studies. Before the statistical results of the simulation in the downstream part of the channel are presented, it is interesting to compare some primary statistics obtained in the inlet section with the fully-developed Couette flow data from Bech et al. (1995) for the same Reynolds number. This is to ensure that the finite-length time series of velocities recycled at the input provided realistic fully-developed turbulence in the upstream section.

In Fig. 2a, the mean velocity profile is plotted at $x/h = 7$ and is nearly indistinguishable from that of Bech et al. (1995). The computed turbulent intensities (the root-mean-square of the velocity fluctuations) are shown in Fig. 2b. The agreement between the two simulations is very good for the wall-normal and streamwise components while the streamwise component exhibits a somewhat higher turbulence level in the present case. This modest difference can be due to different domain sizes and to different grid spacings. The recent DNS of plane Couette flow at the same Reynolds number by Holstad et al. (2010) was performed with a finer mesh in a longer and wider domain. The present results in Fig. 2 are almost indistinguishable from their data.

The Kolmogorov length scale η was estimated from the energy dissipation rate ε as $(\nu^3/\varepsilon)^{1/4}$. The adopted grid spacing turned out to never exceed 2η.

4. Flow structures

In this section, we focus on the instantaneous features of turbulent Couette flow over a backward-facing step. The various plots of the velocity and vorticity fields presented in this section have been non-dimensionalized by U_w and U_w/h, respectively.

4.1. Velocity

A snapshot of the flow field is shown in Fig. 3, where a three-dimensional side view of the iso-surfaces of the streamwise velocity is plotted in Fig. 3a, and a plane parallel to the bottom wall at $y^+ \approx 0.083$ is shown in Fig. 3b. An overall picture of the separation scenario can be deduced from the figure. Starting from the inlet, the incoming flow separates at the sharp step edge and reattaches further downstream leading to the formation of a primary recirculation region. Patches of positive fluid velocity ($u \approx 0.01$) are observed in the region with backward motion ($u < 0$) and adjacent to the step in Fig. 3a, thereby identifying a secondary recirculation region. The interface between the two streams with different velocities leads to a complex three-dimensional flow structure. Fig. 3b provides a qualitative impression of the three-dimensional flow pattern close to the lower-wall. Around $x/h \approx 22$, it is readily observed that the reattachment location is not confined to a fixed streamwise position. Irregular bursts of fluid are formed by the shear-layer at the moment it strikes the bottom plane. Downstream the reattachment, the flow sustains its irregular pattern as it is convected towards the recovery region. Meanwhile, the primary recirculation region shows large structures that are aligned in the spanwise direction with spots of positive fluid velocity observed in-between. These tiny lumps with $u > 0$ are quenched by the surrounding backflow which is driven by the adverse pressure gradient.

A cross-sectional view of the individual velocity fluctuations is shown in Fig. 4. These quantities are defined as the difference between the instantaneous velocity field $\widetilde{u}_i(x, y, z, t)$ and its time-spanwise average $U_i(x, y)$. The results show that fluctuations reach around 20% of the wall velocity U_w in the shear-layer and the primary recirculation zone indicating strong spanwise motions in these regions. The alternating positive–negative pattern observed for v downstream of the step indicates the presence of spanwise vortices. In Fig. 4c, the pseudocolors of w show large elongated structures that are inclined with respect to the streamwise direction and persist into the recovery region almost filling the entire wall gap.

In Fig. 5, we display a top view of iso-surfaces of positive and negative streamwise and spanwise fluctuations. Note that the iso-surfaces of w correspond to the instantaneous spanwise velocity since there is no mean flow in the z-direction. The flow in Fig. 5a clearly features streamwise streaks which are generated in the vicinity of the stepped wall upstream of the corner. These streaky

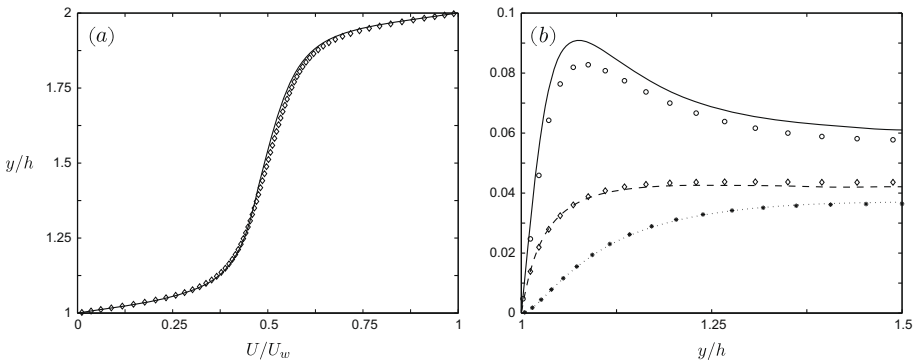

Fig. 2. (a) Mean velocity profile at $x/h = 7$. (b) Turbulent intensities normalized by U_w at $x/h = 7$: ———, streamwise direction; ·····, wall-normal direction; – – – –, spanwise direction. The symbols denote DNS data from Bech et al. (1995).

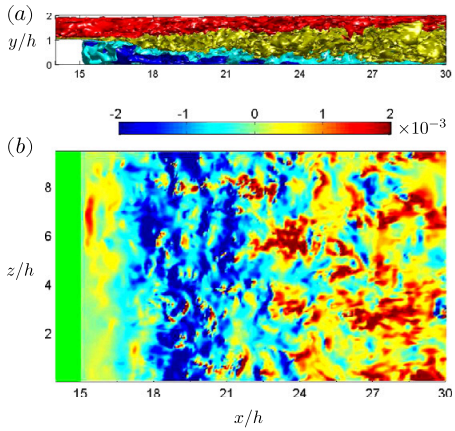

Fig. 3. Instantaneous streamwise velocity. (a) Contour levels: red 0.5, yellow 0.2, cyan 0.01, blue −0.03 and (b) top view at $y^+ = 0.083$.

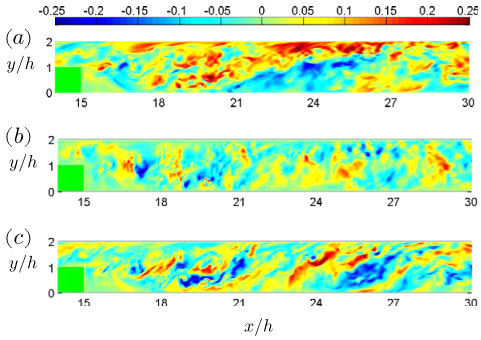

Fig. 4. Instantaneous velocity fluctuations in an (x,y)-plane at $z = L_z/2$. (a) Streamwise component; (b) wall-normal component; (c) spanwise component.

structures grow in width downstream of the step and remain discernible even $15h$ downstream of the corner. In the same region, the iso-surfaces of w show lumps of positive and negative motions. These fluctuations do not exhibit the same streamwise coherence as the streamwise velocity fluctuations.

4.2. Vorticity

Transverse vortices are a commonly observed feature in backward-facing step flows, where the underlying mechanism in the formation of such vortical structures downstream of the step is a Kelvin–Helmholtz instability. These instabilities arise from the interaction between the shear-layer and the recirculating region near the step. This interface between the high- and low-speed fluid region, being unstable, leads to such a vortex formation. In order to see whether or not K–H vortices are embedded in the present flow field, the instantaneous iso-surfaces of enstrophy are plotted in an (x,y)-plane in Fig. 6. There is an apparent roll-up of the shear-layer behind the step edge, where the unsteady K–H vortices are generated and break up into numerous small high-intensity vortices as they are transported downstream.

All turbulent flows exhibit high levels of vorticity fluctuations. The instantaneous vorticity $\widetilde{\omega_i}$ is decomposed into a mean vorticity

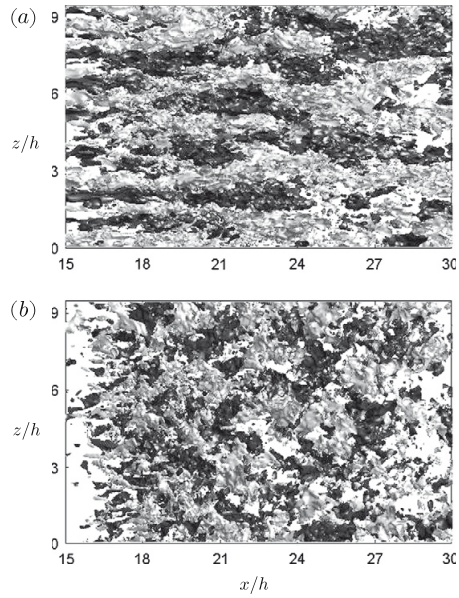

Fig. 5. Top view of iso-surfaces of positive (light) and negative (dark) velocity fluctuations. (a) Streamwise component and (b) spanwise component.

Ω_i and vorticity fluctuations $\omega_i : \widetilde{\omega_i} = \Omega_i + \omega_i,\ \overline{\omega_i} = 0$. The present mean flow is statistically two-dimensional and entirely in the (x,y)-plane. Then Ω_x and Ω_y are zero, so that the only non-zero mean vorticity component is Ω_z. Pseudocolors of vorticity fluctuations are shown in Fig. 7. In contrast with the rather different patterns of the streamwise, wall-normal and spanwise velocity components in Fig. 4, the topology of the three components of the fluctuating vorticity vector in Fig. 7 is rather similar. Since the fluctuating vorticity field is associated with small-scale eddies, the vorticity field is only modestly affected by the anisotropic geometric constraints which enforce a substantial anisotropy on the velocity fluctuations.

A cross-stream view of the vortical structures from $x/h = 15$ is shown in Fig. 8a. These structures are extracted by using the λ_2 definition proposed by Jeong and Hussian (1995) in which a vortex core is identified as a connected region of negative λ_2. Here, λ_2 corresponds to the second largest eigenvalue of the tensor $S_{ij}S_{ij} + \Omega_{ij}\Omega_{ij}$, where S_{ij} and Ω_{ij} represent the symmetric and antisymmetric parts of the velocity gradient tensor, respectively. In the secondary recirculation region large elongated structures are observed in contrast to the upper part of the channel that is filled with numerous small high-intensity vortices. To obtain a more detailed view on the flow in this region, the instantaneous flow in a vertical plane is shown in Fig. 8b at a distance h from the step. The highest turbulent activity is in the shear-layer which is composed of streamwise vortices, whereas in the secondary recirculation region the flow shows surprisingly strong spanwise motions.

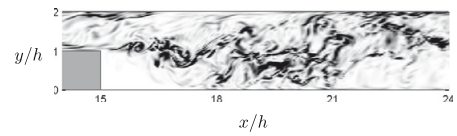

Fig. 6. Instantaneous enstrophy contours in an (x,y)-plane at $z = L_z/2$.

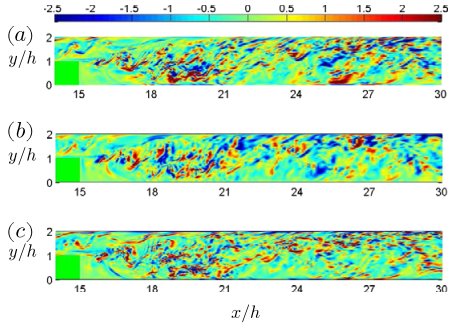

Fig. 7. Instantaneous vorticity fluctuations in an (x,y)-plane at $z = L_z/2$. (a) Streamwise component; (b) wall-normal component; (c) spanwise component.

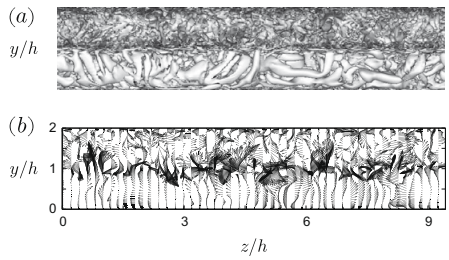

Fig. 8. (a) Cross-stream view of $-\lambda_2$ structures taken from $x/h = 15$. (b) Cross-stream plane at $x/h = 16$. The velocity vectors represent spanwise and wall-normal velocities.

Although the fluid motion in the lee of the step is relatively calm, the flow is by no means laminar.

5. Mean flow and turbulence statistics

The BFS simulation was performed at $Re = 5200$ which led to $Re_{\tau i} \approx 166$ based on the step height h and the upstream friction velocity $u_{\tau i}$. Some comparisons will be made with the hot-wire data of Morinishi (2007) at $Re_{\tau i} \approx 300$ and expansion ratio 3:2.

5.1. Mean statistics

From pressure-driven BFS flows it is known that the unsteady behaviour of the shear-layer causes the reattachment line to fluctuate around a mean value X_R, see e.g. Friedrich and Arnal (1990). The streamline pattern of the mean flow in Fig. 9 shows a large primary separation bubble which extends about $7.5h$ downstream of the step. A secondary bubble of length $1.78h$ can be observed adjacent to the corner. The skin friction coefficient, defined as $C_f = \tau_w / \frac{1}{2}\rho u_{\tau i}^2$, is shown in Fig. 10 and confirms that a secondary separation bubble with anti-clockwise flow ($C_f > 0$) is embedded within the primary separation bubble with clockwise motion ($C_f < 0$). This flow pattern is consistent with the findings of Morinishi (2007) who reported that reattachment occurred at $X_R = 6.63h \pm 1.4h$ and the secondary bubble was at $1.88h \pm 0.4h$. Downstream of $x/h = 30$, C_f is almost constant along both walls, but with the wall-friction along the moving surface being about 10 times higher than at the lower surface. This suggests a substantial asymmetry of the mean velocity field.

The local wall pressure coefficient is defined as

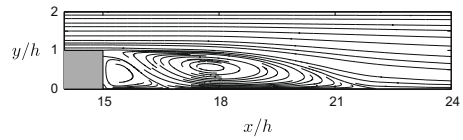

Fig. 9. Streamlines of the mean flow.

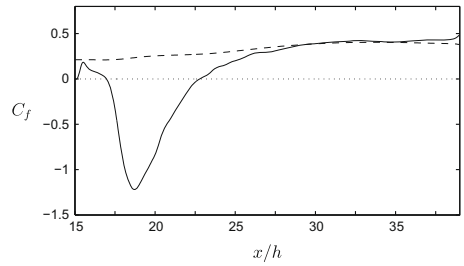

Fig. 10. Skin friction coefficient variation downstream the step: ———, lower-wall; – – – –, upper-wall (divided by a factor of 10).

$$C_p = \frac{P - P_o}{\frac{1}{2}\rho u_{\tau i}^2} \tag{3}$$

where P_o is a reference pressure taken at $x/h = 0$. In Fig. 11, C_p is shown together with the corresponding values from Morinishi (2007) for Couette flow over a backward-facing step. The agreement between the computational and experimental results is very good. The local wall pressure coefficient exhibits a local minimum close to the position of maximum backflow (i.e. beneath the core of the primary separation bubble), just as in the pressure-driven BFS flow; Barri et al. (2010). Downstream of $x/h = 30$, an almost linear variation of C_p is observed for the two cases. This implies that the streamwise mean pressure gradient has become independent of x, in keeping with the measurements of Morinishi (2007), and the flow field can be considered as being nearly fully-developed in the downstream part of the computational domain. This is also consistent with the constancy of C_f observed in Fig. 10.

The mean velocity profiles are presented in Figs. 12 and 13 for the streamwise and wall-normal components at different representative locations: inside the secondary bubble, through the primary recirculation, downstream of the reattachment and in the recovery region. In the recirculation region the strongest backflow is observed beneath the core of the primary bubble, whereas the secondary separation region shows a weak mean-streamwise

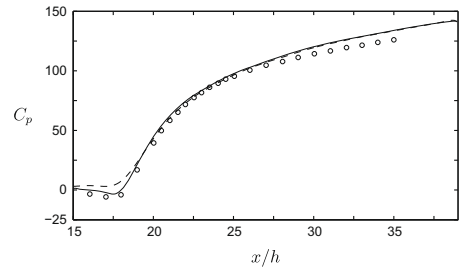

Fig. 11. Pressure coefficient variation downstream the step: ———, lower-wall; – – – –, upper-wall. The symbols denote lower-wall data from Morinishi (2007), case C300.

motion. Although the characteristic S-shape of the mean velocity profile $U(x,y)$ has been retained at $x/h = 27$, the profile is yet far from being anti-symmetric. Midway between the walls U is still roughly half of $U_w/2$ which should have been reached in the case a fully redeveloped Couette flow. However, irrespective of the length of the domain that can be used in the downstream part of the channel, an anti-symmetric profile corresponding to a fully redeveloped Couette flow will not be reached. This is due to the principle of mass conservation. It follows that since the height of the domain after the step is twice that of the inlet section and the mean velocity profile of Couette flow is monotonically increasing to a constant value of U_w, the flow cannot adjust itself to an anti-symmetric S-profile shape and at the same time maintain a constant flow rate.

An examination of the mean wall-normal velocity profiles $V(x,y)$ presented in Fig. 13 shows that the flow emanating from the step corner exhibits an upward motion in the lower half of the channel and a downward flow above $y/h \approx 1$. The distinct positive V at $x/h = 16$ results from the primary recirculation bubble, in which the return flow has separated from the wall at $x/h \approx 16.8$. This pattern is sustained up till $x/h \approx 18$, where afterwards a relatively strong downward motion is solely observed above the remaining part of the recirculation zone. Downstream of the reattachment region, the mean wall-normal velocity is attenuated.

5.2. Turbulence intensities and Reynolds shear stress

The turbulence intensities and the Reynolds shear stress are shown in Figs. 14 and 15 at different streamwise locations downstream the step. The *rms* values and $-\overline{u}\overline{v}$ exhibit a high turbulence level immediately downstream of the corner of the step at $y/h \approx 1$. This localized high-turbulence zone, mainly for u_{rms}, is obviously caused by the locally high mean-shear-rate in the shear-layer emanating from the step edge. As the flow progresses downstream, the streamwise turbulence intensity peaks are broadened and attenuated while the turbulence levels of the spanwise and wall-normal components increase. Downstream the reattachment and in the recovery region, the asymmetry in u_{rms} persists, where a substantially higher longitudinal turbulence intensity is observed near the moving wall that is almost twice that seen near the stationary wall. Apart from the secondary recirculation region, where $w_{rms} > u_{rms} > v_{rms}$, the turbulence exhibits everywhere the usual shear-flow anisotropy with the streamwise intensity being the most significant. The flow anisotropy was not accessible with the I-type hot-wire used in Morinishi's (2007) measurements since only u_{rms} could be obtained.

The profiles of $-\overline{u}\overline{v}$ show that the Reynolds shear stress is positive almost throughout the whole domain. The distinct positive peak of $-\overline{u}\overline{v}$ is typical of a turbulent mixing-layer. The peak broadens with downstream distance but remains discernible above the

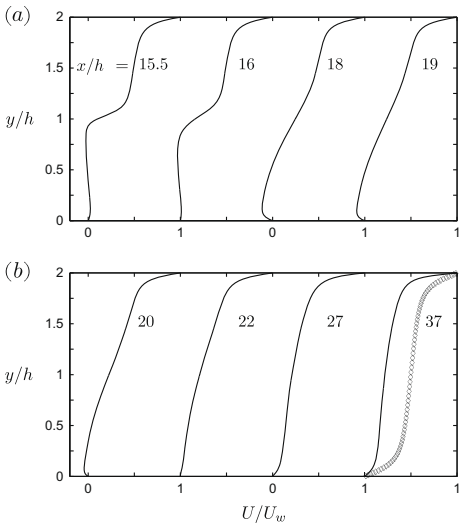

Fig. 12. Mean streamwise velocity profiles. (a) Recirculation region and (b) recirculation, reattachment and recovery regions.

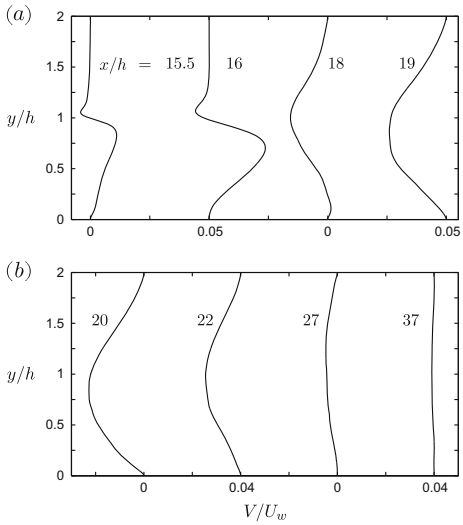

Fig. 13. Mean wall-normal velocity profiles. (a) Recirculation region and (b) recirculation, reattachment and recovery regions.

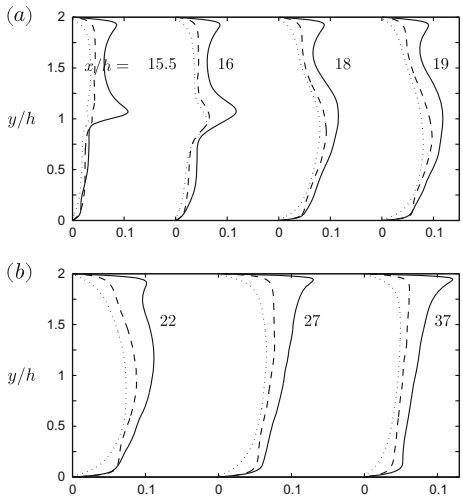

Fig. 14. Turbulent intensities scaled with the maximum mean velocity at the input: ———, streamwise direction; ·····, wall-normal direction; – – – –, spanwise direction. (a) Recirculation region and (b) reattachment and recovery regions.

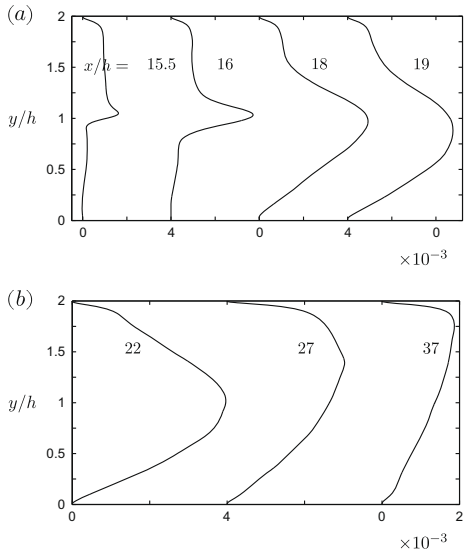

Fig. 15. Reynolds shear stress $-\overline{uv}/U_w^2$. (a) Recirculation region and (b) reattachment and recovery regions.

reattachment point at about $7h$ downstream of the step. Further downstream, the $-\overline{uv}$-profile fails to attain the symmetric shape which characterizes a pure Couette flow; see e.g. Bech and Andersson (1996). The profile at $x/h = 37$, i.e. 22 step heights downstream of the step, shows that the Reynolds shear stress is substantially higher near the moving wall than along the fixed wall.

5.3. Reynolds stress budget

In this section, the Reynolds stress budget is presented at a distance h from the step and in a wall-normal region confined to the shear-layer region (i.e. $0.5 < y/h < 1.5$). The transport equation for the Reynolds stress tensor is:

$$\frac{D}{Dt}(\overline{u_i u_j}) = P_{ij} - \varepsilon_{ij} + \Pi_{ij} + G_{ij} + D_{ij} + T_{ij} \tag{4}$$

where the production, dissipation, pressure–strain, pressure diffusion, molecular diffusion and turbulent diffusion are defined as:

$$P_{ij} = -\overline{u_i u_k}\frac{\partial U_j}{\partial x_k} - \overline{u_j u_k}\frac{\partial U_i}{\partial x_k} \tag{5a}$$

$$\varepsilon_{ij} = 2\nu\overline{\frac{\partial u_i}{\partial x_k}\frac{\partial u_j}{\partial x_k}} \tag{5b}$$

$$\Pi_{ij} = \frac{1}{\rho}\left(\overline{p\frac{\partial u_i}{\partial x_j}} + \overline{p\frac{\partial u_j}{\partial x_i}}\right) \tag{5c}$$

$$G_{ij} = -\frac{1}{\rho}\left(\frac{\partial}{\partial x_i}\overline{pu_j} + \frac{\partial}{\partial x_j}\overline{pu_i}\right) \tag{5d}$$

$$D_{ij} = \nu\frac{\partial^2}{\partial x_k^2}\overline{u_i u_j} \tag{5e}$$

$$T_{ij} = -\frac{\partial}{\partial x_k}\overline{u_i u_j u_k} \tag{5f}$$

The budget for $\overline{uu}$ in Fig. 16a is largely dominated by production and pressure–strain, where a large peak of positive production is observed close to the position of maximum u_{rms} (i.e. $y/h \approx 1$). Meanwhile, the profiles of the molecular diffusion in Fig. 16 show that the contribution of D_{ij} is negligible everywhere and thereby turbulent and pressure diffusion play the role of transporting energy across the shear-layer. For the normal stresses, T_{ij} carries energy away from the position of maximum production.

The mean-shear production P_{22} in Fig. 16b is clearly smaller than P_{11} in Fig. 16a, but nevertheless far from being negligible as in free shear flows. In the present case P_{22} stems from $-\overline{vv}\partial V/\partial y$, which attains non-vanishing levels due to the underlying recirculating flow; see the V-profile in Fig. 13a. Since there is only modest production of $\overline{v^2}$, the primary source of energy is from Π_{ij} which serves to redistribute energy between the normal stresses. Across the entire shear-layer, $\overline{vv}$ and $\overline{ww}$ act as receiving components taking energy from $\overline{uu}$. Moreover, the maximum rate of energy transfer is reported at the peak production for the streamwise normal stress.

As in the budget of $\overline{uu}$, the equation for $\overline{uv}$ is largely dominated by production and pressure–strain, where a large peak of negative production is observed around $y/h = 1$. The expression for this production term is

$$P_{12} = -\overline{uv}\frac{\partial U}{\partial x} - \overline{vv}\frac{\partial U}{\partial y} - \overline{uu}\frac{\partial V}{\partial x} - \overline{uv}\frac{\partial V}{\partial y} \tag{6}$$

Since the mean flow is statistically two-dimensional, the first and fourth terms of Eq. (6) add up to zero due to mass conservation. This implies that the sign of P_{12} depends solely on the gradients of the mean streamwise and wall-normal velocities. Since $\partial U/\partial y$ being dominant over all the other mean gradient terms in this region, then Eq. (6) reduces to $P_{12} \approx -\overline{vv}\partial U/\partial y$. The production of the Reynolds shear stress is thus governed by $\partial U/\partial y$ and peak production is attained, where $\partial U/\partial y$ exhibits a local maximum in the shear-layer. This is consistent with a free mixing-layer.

The turbulent diffusion T_{12} contributes to the increase of $\overline{uv}$ in the central region whereas pressure diffusion G_{12} transports $\overline{uv}$ downwards from the upper part of the shear-layer. Meanwhile, viscous dissipation is negligible almost everywhere in this case. The nearly negligible viscous dissipation is consistent with the observation made by Bech and Andersson (1996) in a fully-developed Couette flow. This is because ε_{12} consists of relatively weakly correlated velocity gradients $\partial u_1/\partial x_k$ and $\partial u_2/\partial x_k$. This is in contrast to the diagonal components of ε_{ij} which do not involve cross-correlations.

Although the convection term $U_k\partial(\overline{u_i u_j})/\partial x_k$ is almost negligible for the stress components dominated by production (i.e. $\overline{uu}$ and $\overline{uv}$), it shows significant positive values in the shear-layer for the wall-normal and spanwise components. In fact, the convective transport of $\overline{ww}$ is equally important as its dissipation rate ε_{33}.

5.4. Recovery region

The two-dimensional mean flow has developed to an essentially unidirectional flow in the downstream part of the computational domain, i.e. beyond $x/h \approx 30$ or 15 step heights h downstream of the sudden expansion. It is noteworthy that the upstream pure Couette flow redeveloped into a mixed Couette–Poiseuille flow in contrast to the classical pressure-driven backward-facing step flow, where an upstream Poiseuille flow inevitably redevelops to another pure Poiseuille flow far downstream of the step. In the present case, however, an adverse pressure gradient is established with the view to assure global mass conservation. The resulting mixed Couette–Poiseuille flow exhibits major asymmetries in the turbulence field with a substantially reduced turbulence level along the stationary wall, and the flow field closely resembles the Couette–Poiseuille flow simulations reported by Kuroda et al. (1995).

Kuroda et al. (1995) conducted direct numerical simulations of fully-developed turbulent plane Couette–Poiseuille flow to study the effect of the mean-shear-rate on the near-wall turbulent flow

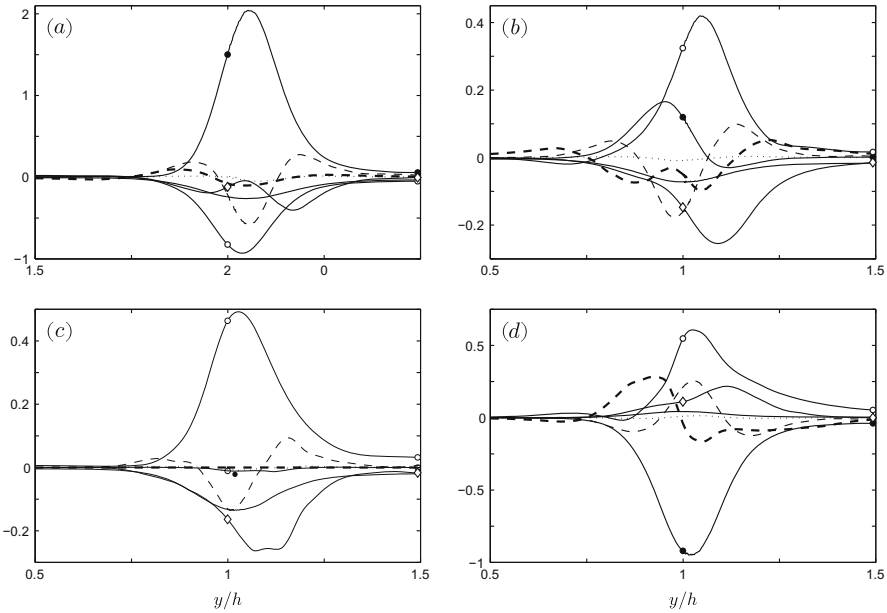

Fig. 16. Reynolds stress budget normalized by $u_{\tau i}^4/\nu$ at $x/h = 16$. -●-, P_{ij}; ——, $-\varepsilon_{ij}$; -○-, Π_{ij}; ——————, G_{ij}; ·····, D_{ij}; – – – –, T_{ij}; -◇-, $-U_k\partial(\overline{u_iu_j})/\partial x_k$. (a) $\overline{uu}$; (b) $\overline{vv}$; (c) $\overline{ww}$; (d) $\overline{uv}$.

field. Four cases were considered by these authors in which the mean-shear-rate was varied by changing the wall velocity and the streamwise pressure gradient. Of particular relevance to our study is case *CP*3 in Kuroda et al. (1995).

Owing to the asymmetry of the Couette–Poiseuille flow, the wall shear stresses on the lower and upper-wall are generally different. For the current simulation, the corresponding local Reynolds numbers based on the local wall friction-velocities and the non-dimensionalized pressure gradient are provided in Table 2 together with simulation parameters from Kuroda et al. (1995). The mean velocity profile and turbulent intensities presented in Fig. 17 compare surprisingly well with the DNS data of Kuroda et al. (1995), especially near the upper-wall. However, substantial differences are observed near the lower-wall. The streamwise turbulence intensity, for instance, exhibits a modest peak in the present case, whereas a monotonic increase towards the peak near the upper-wall is exhibited by the DNS data of Kuroda et al. (1995). The rather different behaviour in the vicinity of the lower-wall is due to the almost vanishing friction velocity $u_{\tau b}$ in the latter case. At $x/h = 37$ in the present case, the friction velocity is substantially reduced by the adverse pressure gradient but yet of sufficient magnitude to give rise to mean-shear production of streamwise velocity fluctuations. The Reynolds stress budget presented by Kuroda et al. (1995) indeed showed that mean-shear production only plays a marginal role near the lower-wall.

Table 2
Simulation parameters from Kuroda et al. (1995) case *CP*3, and present simulation at $x/h = 37$. Here, $c = +H/2\rho U_w^2$. The subscripts t and b refer to the top and bottom walls, respectively.

Case	$U_wH/2\nu$	$c \times \partial P/\partial x$	$u_{\tau t}H/2\nu$	$u_{\tau b}H/2\nu$
Kuroda	3000	-1.33×10^{-3}	154	17.7
Present	5200	1.2×10^{-3}	233.8	77

5.5. Vorticity and λ_2 statistics

Profiles of the root-mean-square vorticity normalized by $u_{\tau i}^2/\nu$ are shown in Fig. 18. While the secondary recirculation region in Fig. 18a shows low levels, the effect of mean-shear motion is clearly observed above $y/h \approx 0.75$ in the form of increasing vorticity fluctuations. This increase is sustained till midway between the walls, where the three components attain their local maxima in the shear-layer, followed by a decrease towards a local minimum around $y/h \approx 1.5$. Two step heights further downstream, the primary recirculation region in Fig. 18b shows higher fluctuation levels than the secondary one while in the shear-layer $(\overline{\omega_x^2})^{1/2}$ is amplified and $(\overline{\omega_z^2})^{1/2}$ is attenuated. In a direct numerical simulation of a self-similar mixing-layer Rogers and Moser (1993), reported an axisymmetric anisotropy in the free planar shear-layer. In the present case, however, the results show that the vorticity is almost isotropic in the shear-layer. Near the upper-wall however, the distributions of $(\overline{\omega_i^2})^{1/2}$ are highly anisotropic as in the case of plane Couette flow, whereas at the stationary wall a different anisotropy is observed with $(\overline{\omega_x^2})^{1/2}$ and $(\overline{\omega_z^2})^{1/2}$ being almost equal and attaining higher values than $(\overline{\omega_y^2})^{1/2}$. It is noteworthy that the flow exhibits the same anisotropy further downstream. The wall-normal vorticity fluctuations inevitably vanish at both walls due to the no-slip conditions. The local near-wall peak of $(\overline{\omega_x^2})^{1/2}$, which is associated with streamwise-oriented vortices, is absent along the fixed wall.

Fig. 19 shows the cross-correlation between $-\lambda_2$ and the three components of the vorticity fluctuation vector in the recirculation and recovery regions. The main tendency at both x-stations is that the cross-correlation between $-\lambda_2$ and ω_x is higher than that between $-\lambda_2$, ω_y and ω_z. This indicates that the turbulent vortices are predominantly aligned in the streamwise direction, even though the fluctuating vorticity field, associated with the small-scale turbulence, is close to isotropy.

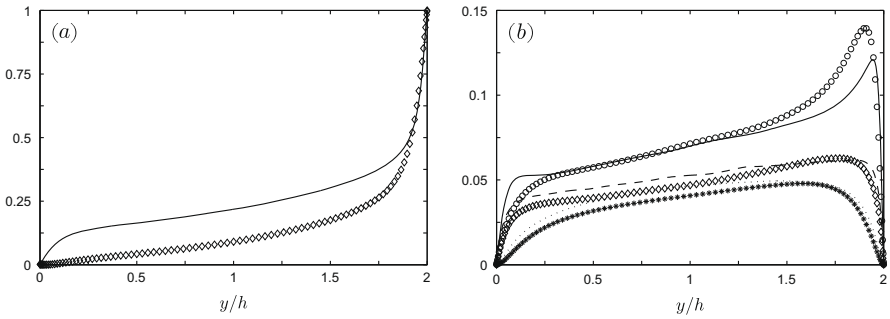

Fig. 17. (a) Mean velocity profile U/U_w at $x/h = 37$. (b) Turbulent intensities at $x/h = 37$: ———, ∘, streamwise direction; ·····, ∗, wall-normal direction; – – – –, ♢, spanwise direction. The symbols denote DNS data from Kuroda et al. (1995).

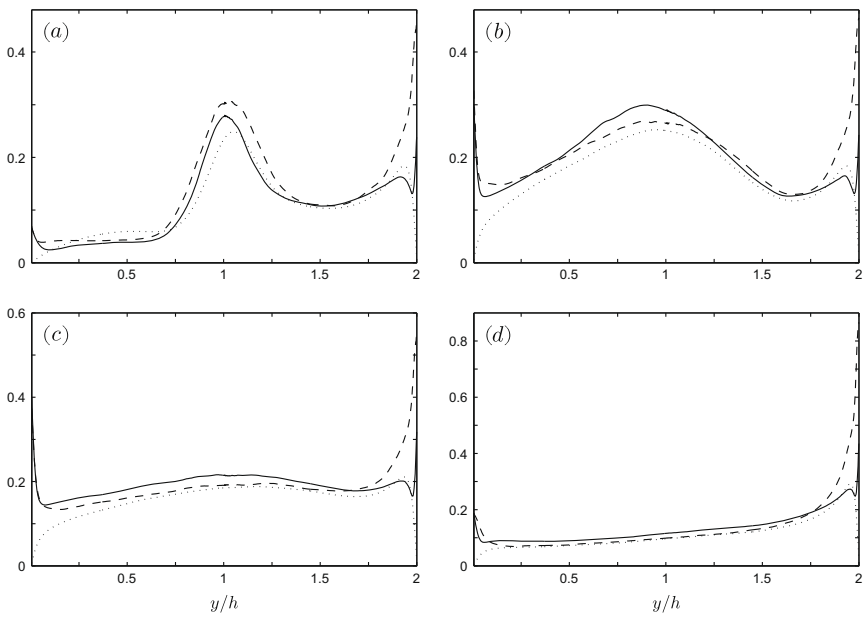

Fig. 18. Wall-normal distribution of the root-mean-square vorticity fluctuations normalized by $u_{\tau i}^2/\nu$: ———, streamwise direction; ·····, wall-normal direction; – – – –, spanwise direction. (a) $x/h = 16$; (b) $x/h = 18$; (c) $x/h = 22$; (d) $x/h = 37$.

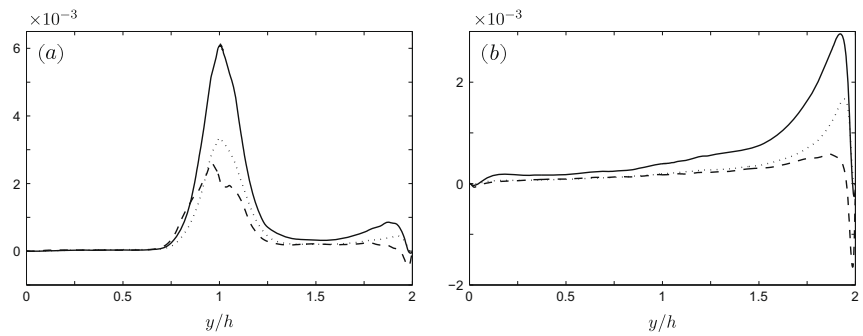

Fig. 19. Wall-normal distribution of the dimensionless cross-correlation of $-\lambda_2$ with ω_i normalized by $u_{\tau i}^6/\nu^3$: ———, $\overline{-\lambda_2\omega_x}$; ·····, $\overline{-\lambda_2\omega_y}$; – – – –, $\overline{-\lambda_2\omega_z}$. (a) $x/h = 16$ and (b) $x/h = 37$.

6. Conclusions

A direct numerical simulation of turbulent Couette flow over a backward-facing step has been performed at a relatively low Reynolds number. The mean reattachment length of the shear-layer was found to be 7.5h. In the recirculation zone a large negative skin friction coefficient was observed beneath the core of the primary separation bubble.

The streaky near-wall structures formed along the step persisted several step heights downstream of the step. High and anisotropic turbulence levels were produced in the shear-layer emanating from the corner. Although advection by the mean flow as well as turbulent diffusion were of some importance in the vicinity of the step, the mean-shear production was the primary source of turbulent energy. As in other turbulent shear flows, the energy arose as streamwise velocity fluctuations and was subsequently transferred into wall-normal and spanwise fluctuations by means of pressure–strain interactions.

The shear-layer which formed when the upstream Couette flow mixed with the recirculating flow downstream of the step resembles, at least qualitatively, a free mixing-layer in many respects. However, the turbulence in the approaching Couette flow is convected into the early stages of the mixing zone, where also the "upwelling" caused by the primary separation bubble has a major influence. Beyond 3h downstream of the corner, the mean flow turns towards the reattachment point and the shear-layer is simultaneously affected by the streamwise curvature and an adverse mean pressure gradient. The shear-layer which develops from the corner of the BFS is accordingly exposed to a number of different influences not present in a freely developing mixing-layer.

Even though the wall-normal mean velocity V vanished far downstream of the step, the streamwise velocity U did not retain the characteristic S-shape typical of a pure Couette flow. This phenomenon is ascribed to the principle of global mass conservation, which can be fulfilled only if an adverse mean pressure gradient is established in the recovery region. This is indeed what was observed. In the resulting asymmetric mean flow, the wall-friction was roughly 10 times higher along the moving wall than at the steady surface. The resulting flow field was thus by far less vigorous along the stepped wall and this was reflected in the low levels of velocity and vorticity fluctuations.

Acknowledgements

We are grateful to the audience at the 6th International Symposium on Turbulence and Shear Flow Phenomena in Seoul (June 2009) for the constructive comments and valuable feedback on the presentation of this work by the first author.

PhD research fellowships for the first and third authors were provided by the Norwegian University of Science and Technology (NTNU) and the Research Council of Norway, respectively.

Computing time was granted by the Research Council of Norway (Programme for Supercomputing) and by the Research Programme in Computational Science and Visualization (BVV) at NTNU.

References

Abbot, D.E., Kline, S.J., 1962. Experimental investigations of subsonic turbulent flow over single and double backward-facing steps. Trans. A.S.M.E. D: J. Basic Eng. 84, 317–325.

Armaly, B.F., Durst, F., Pereira, J.C.F., Schönung, B., 1983. Experimental and theoretical investigation of backward-facing step flow. J. Fluid Mech. 127, 473–496.

Barri, M., El Khoury, G.K., Andersson, H.I., Pettersen, B., 2009. Inflow conditions for inhomogeneous turbulent flows. Int. J. Numer. Meth. Fluids 60, 227–235.

Barri, M., El Khoury, G.K., Andersson, H.I., Pettersen, B., 2010. DNS of backward-facing step flow with fully turbulent inflow. Int. J. Numer. Meth. Fluids. doi:10.1002/fld.2176.

Bech, K.H., Tillmark, N., Alfredsson, P.H., Andersson, H.I., 1995. An investigation of turbulent plane Couette flow at low Reynolds numbers. J. Fluid Mech. 286, 291–325.

Bech, K.H., Andersson, H.I., 1996. Structure of Reynolds shear stress in the central region of plane Couette flow. Fluid Dynam. Res. 18, 65–79.

Durst, F., Tropea, C., 1981. Turbulent backward-facing step flows in two-dimensional ducts and channels. In: Proc. Third Intl. Symp. on Turbulent Shear Flows, pp. 18.1–18.5.

Eaton, J.K., Johnston, J.P., 1981. A review of research on subsonic turbulent flow reattachment. AIAA J. 19, 1093–1100.

Friedrich, R., Arnal, M., 1990. Analysing turbulent backward-facing step flow with the lowpass-filtered Navier–Stokes equations. J. Wind Eng. Ind. Aerodyn. 35, 101–128.

Goldstein, R.J., Eriksen, V.L., Olson, R.M., Eckert, E.R.G., 1970. Laminar separation reattachment, and transition of flow over a downstream-facing step. Trans. A.S.M.E. D: J. Basic Eng. 92, 732–741.

Holstad, A., Andersson, H.I., Pettersen, B., 2010. Turbulence in a three-dimensional wall-bounded shear flow. Int. J. Numer. Meth. Fluids 62, 875–905.

Jeong, J., Hussian, F., 1995. On the identification of a vortex. J. Fluid Mech. 285, 69–94.

Kuehn, D.M., 1980. Some effects of adverse pressure gradient on the incompressible reattaching flow over a rearward-step. AIAA J. 18, 343–344.

Kuroda, A., Kasagi, N., Hirata, M., 1995. Direct numerical simulation of turbulent plane Couette–Poiseuille flows: effect of mean shear rate on the near-wall turbulence structures. Turbulent Shear Flows, vol. 9, Springer-Verlag, Berlin, pp. 240–257.

Le, H., Moin, P., Kim, J., 1997. Direct numerical simulation of turbulent flow over a backward-facing step. J. Fluid Mech. 330, 349–374.

Lowery, P.S., Reynolds, W.C., 1986. Numerical Simulation of a Spatially-developing, Forced, Plane Mixing Layer. Rep. TF-26. Thermosciences Division, Department of Mechanical Engineering, Stanford University.

Manhart, M., 2004. A zonal algorithm for DNS of turbulent boundary layers. Comput. Fluids 33, 435–461.

Meri, A., Wengle, H., 2002. DNS and LES of turbulent backward-facing step flow using 2nd- and 4th-order discretization. In: Friedrich, R., Rodi, W. (Eds.), Advances in LES of Complex Flows, vol. 65. Kluwer Academic Publishers, pp. 99–114.

Morinishi, Y., 2007. Backward-facing step flow between step-side stationary and moving walls. In: Proc. 5th International Symposium on Turbulence and Shear Flow Phenomena, Munich, pp. 673–676.

Neto, S.A., Grand, D., Métais, O., Lesieur, M., 1993. A numerical investigation of the coherent vortices in turbulence behind a backward-facing step. J. Fluid Mech. 256, 1–25.

Ötügen, M.V., 1991. Expansion ratio effects on the separated shear layer and reattachment downstream of a backward-facing step. Exp. Fluids 10, 273–280.

Ra, S.H., Chang, P.K., 1990. Effects of pressure gradient on reattaching flow downstream of a rearward-facing step. J. Aircraft 27, 93–95.

Rogers, M.M., Moser, R.D., 1993. Direct simulation of a self similar turbulent mixing layer. Phys. Fluids 6, 903–923.

Spalart, P.R., 1988. Direct simulation of a turbulent boundary layer up to $Re_\theta = 1410$. J. Fluid Mech. 187, 61–98.

Paper 3

Asymmetries in an obstructed turbulent channel flow

El Khoury, G. K., Pettersen, B., Andersson, H. I. & Barri, M.

Physics of Fluids **22**, 095103–13, 2010.

Is not included due to copyright

Part 2.2

Bluff body flows

Paper 4

Wakes behind a prolate spheroid in crossflow

El Khoury, G. K., Andersson, H. I. & Pettersen, B.

Submitted to *Journal of Fluid Mechanics*.

Is not included due to copyright

Paper 5

Crossflow past a prolate spheroid at Reynolds number of 10 000

El Khoury, G. K., Andersson, H. I. & Pettersen, B.

Journal of Fluid Mechanics **659**, 365–374, 2010.

Is not included due to copyright

Appendix

Paper 6

Simulating turbulent Dean flow in Cartesian coordinates

El Khoury, G. K., Andersson, H. I. & Pettersen, B.

International Journal for Numerical Methods in Fluids **60**, 263–274, 2009.

Is not included due to copyright

Paper 7

DNS of backward-facing step flow with fully turbulent inflow

Barri, M., El Khoury, G. K., Andersson, H. I. & Pettersen, B.

International Journal for Numerical Methods in Fluids **64**, 777–792, 2010.

Is not included due to copyright

R A P P O R T E R
UTGITT VED
INSTITUTT FOR MARIN TEKNIKK
(tidligere: FAKULTET FOR MARIN TEKNIKK)
NORGES TEKNISK-NATURVITENSKAPELIGE UNIVERSITET

Report No.	Author	Title
	Kavlie, Dag	Optimization of Plane Elastic Grillages, 1967
	Hansen, Hans R.	Man-Machine Communication and Data-Storage Methods in Ship Structural Design, 1971
	Gisvold, Kaare M.	A Method for non-linear mixed -integer programming and its Application to Design Problems, 1971
	Lund, Sverre	Tanker Frame Optimalization by means of SUMT-Transformation and Behaviour Models, 1971
	Vinje, Tor	On Vibration of Spherical Shells Interacting with Fluid, 1972
	Lorentz, Jan D.	Tank Arrangement for Crude Oil Carriers in Accordance with the new Anti-Pollution Regulations, 1975
	Carlsen, Carl A.	Computer-Aided Design of Tanker Structures, 1975
	Larsen, Carl M.	Static and Dynamic Analysis of Offshore Pipelines during Installation, 1976
UR-79-01	Brigt Hatlestad, MK	The finite element method used in a fatigue evaluation of fixed offshore platforms. (Dr.Ing. Thesis)
UR-79-02	Erik Pettersen, MK	Analysis and design of cellular structures. (Dr.Ing. Thesis)
UR-79-03	Sverre Valsgård, MK	Finite difference and finite element methods applied to nonlinear analysis of plated structures. (Dr.Ing. Thesis)
UR-79-04	Nils T. Nordsve, MK	Finite element collapse analysis of structural members considering imperfections and stresses due to fabrication. (Dr.Ing. Thesis)
UR-79-05	Ivar J. Fylling, MK	Analysis of towline forces in ocean towing systems. (Dr.Ing. Thesis)
UR-80-06	Nils Sandsmark, MM	Analysis of Stationary and Transient Heat Conduction by the Use of the Finite Element Method. (Dr.Ing. Thesis)
UR-80-09	Sverre Haver, MK	Analysis of uncertainties related to the stochastic modeling of ocean waves. (Dr.Ing. Thesis)
UR-81-15	Odland, Jonas	On the Strength of welded Ring stiffened cylindrical Shells primarily subjected to axial Compression

UR-82-17	Engesvik, Knut	Analysis of Uncertainties in the fatigue Capacity of Welded Joints
UR-82-18	Rye, Henrik	Ocean wave groups
UR-83-30	Eide, Oddvar Inge	On Cumulative Fatigue Damage in Steel Welded Joints
UR-83-33	Mo, Olav	Stochastic Time Domain Analysis of Slender Offshore Structures
UR-83-34	Amdahl, Jørgen	Energy absorption in Ship-platform impacts
UR-84-37	Mørch, Morten	Motions and mooring forces of semi submersibles as determined by full-scale measurements and theoretical analysis
UR-84-38	Soares, C. Guedes	Probabilistic models for load effects in ship structures
UR-84-39	Aarsnes, Jan V.	Current forces on ships
UR-84-40	Czujko, Jerzy	Collapse Analysis of Plates subjected to Biaxial Compression and Lateral Load
UR-85-46	Alf G. Engseth, MK	Finite element collapse analysis of tubular steel offshore structures. (Dr.Ing. Thesis)
UR-86-47	Dengody Sheshappa, MP	A Computer Design Model for Optimizing Fishing Vessel Designs Based on Techno-Economic Analysis. (Dr.Ing. Thesis)
UR-86-48	Vidar Aanesland, MH	A Theoretical and Numerical Study of Ship Wave Resistance. (Dr.Ing. Thesis)
UR-86-49	Heinz-Joachim Wessel, MK	Fracture Mechanics Analysis of Crack Growth in Plate Girders. (Dr.Ing. Thesis)
UR-86-50	Jon Taby, MK	Ultimate and Post-ultimate Strength of Dented Tubular Members. (Dr.Ing. Thesis)
UR-86-51	Walter Lian, MH	A Numerical Study of Two-Dimensional Separated Flow Past Bluff Bodies at Moderate KC-Numbers. (Dr.Ing. Thesis)
UR-86-52	Bjørn Sortland, MH	Force Measurements in Oscillating Flow on Ship Sections and Circular Cylinders in a U-Tube Water Tank. (Dr.Ing. Thesis)
UR-86-53	Kurt Strand, MM	A System Dynamic Approach to One-dimensional Fluid Flow. (Dr.Ing. Thesis)
UR-86-54	Arne Edvin Løken, MH	Three Dimensional Second Order Hydrodynamic Effects on Ocean Structures in Waves. (Dr.Ing. Thesis)
UR-86-55	Sigurd Falch, MH	A Numerical Study of Slamming of Two-Dimensional Bodies. (Dr.Ing. Thesis)
UR-87-56	Arne Braathen, MH	Application of a Vortex Tracking Method to the Prediction of Roll Damping of a Two-Dimension

		Floating Body. (Dr.Ing. Thesis)
UR-87-57	Bernt Leira, MK	Gaussian Vector Processes for Reliability Analysis involving Wave-Induced Load Effects. (Dr.Ing. Thesis)
UR-87-58	Magnus Småvik, MM	Thermal Load and Process Characteristics in a Two-Stroke Diesel Engine with Thermal Barriers (in Norwegian). (Dr.Ing. Thesis)
MTA-88-59	Bernt Arild Bremdal, MP	An Investigation of Marine Installation Processes – A Knowledge - Based Planning Approach. (Dr.Ing. Thesis)
MTA-88-60	Xu Jun, MK	Non-linear Dynamic Analysis of Space-framed Offshore Structures. (Dr.Ing. Thesis)
MTA-89-61	Gang Miao, MH	Hydrodynamic Forces and Dynamic Responses of Circular Cylinders in Wave Zones. (Dr.Ing. Thesis)
MTA-89-62	Martin Greenhow, MH	Linear and Non-Linear Studies of Waves and Floating Bodies. Part I and Part II. (Dr.Techn. Thesis)
MTA-89-63	Chang Li, MH	Force Coefficients of Spheres and Cubes in Oscillatory Flow with and without Current. (Dr.Ing. Thesis
MTA-89-64	Hu Ying, MP	A Study of Marketing and Design in Development of Marine Transport Systems. (Dr.Ing. Thesis)
MTA-89-65	Arild Jæger, MH	Seakeeping, Dynamic Stability and Performance of a Wedge Shaped Planing Hull. (Dr.Ing. Thesis)
MTA-89-66	Chan Siu Hung, MM	The dynamic characteristics of tilting-pad bearings
MTA-89-67	Kim Wikstrøm, MP	Analysis av projekteringen for ett offshore projekt. (Licenciat-avhandling)
MTA-89-68	Jiao Guoyang, MK	Reliability Analysis of Crack Growth under Random Loading, considering Model Updating. (Dr.Ing. Thesis)
MTA-89-69	Arnt Olufsen, MK	Uncertainty and Reliability Analysis of Fixed Offshore Structures. (Dr.Ing. Thesis)
MTA-89-70	Wu Yu-Lin, MR	System Reliability Analyses of Offshore Structures using improved Truss and Beam Models. (Dr.Ing. Thesis)
MTA-90-71	Jan Roger Hoff, MH	Three-dimensional Green function of a vessel with forward speed in waves. (Dr.Ing. Thesis)
MTA-90-72	Rong Zhao, MH	Slow-Drift Motions of a Moored Two-Dimensional Body in Irregular Waves. (Dr.Ing. Thesis)
MTA-90-73	Atle Minsaas, MP	Economical Risk Analysis. (Dr.Ing. Thesis)
MTA-90-74	Knut-Aril Farnes, MK	Long-term Statistics of Response in Non-linear Marine Structures. (Dr.Ing. Thesis)
MTA-90-	Torbjørn Sotberg, MK	Application of Reliability Methods for Safety

75		Assessment of Submarine Pipelines. (Dr.Ing. Thesis)
MTA-90-76	Zeuthen, Steffen, MP	SEAMAID. A computational model of the design process in a constraint-based logic programming environment. An example from the offshore domain. (Dr.Ing. Thesis)
MTA-91-77	Haagensen, Sven, MM	Fuel Dependant Cyclic Variability in a Spark Ignition Engine - An Optical Approach. (Dr.Ing. Thesis)
MTA-91-78	Løland, Geir, MH	Current forces on and flow through fish farms. (Dr.Ing. Thesis)
MTA-91-79	Hoen, Christopher, MK	System Identification of Structures Excited by Stochastic Load Processes. (Dr.Ing. Thesis)
MTA-91-80	Haugen, Stein, MK	Probabilistic Evaluation of Frequency of Collision between Ships and Offshore Platforms. (Dr.Ing. Thesis)
MTA-91-81	Sødahl, Nils, MK	Methods for Design and Analysis of Flexible Risers. (Dr.Ing. Thesis)
MTA-91-82	Ormberg, Harald, MK	Non-linear Response Analysis of Floating Fish Farm Systems. (Dr.Ing. Thesis)
MTA-91-83	Marley, Mark J., MK	Time Variant Reliability under Fatigue Degradation. (Dr.Ing. Thesis)
MTA-91-84	Krokstad, Jørgen R., MH	Second-order Loads in Multidirectional Seas. (Dr.Ing. Thesis)
MTA-91-85	Molteberg, Gunnar A., MM	The Application of System Identification Techniques to Performance Monitoring of Four Stroke Turbocharged Diesel Engines. (Dr.Ing. Thesis)
MTA-92-86	Mørch, Hans Jørgen Bjelke, MH	Aspects of Hydrofoil Design: with Emphasis on Hydrofoil Interaction in Calm Water. (Dr.Ing. Thesis)
MTA-92-87	Chan Siu Hung, MM	Nonlinear Analysis of Rotordynamic Instabilities in Highspeed Turbomachinery. (Dr.Ing. Thesis)
MTA-92-88	Bessason, Bjarni, MK	Assessment of Earthquake Loading and Response of Seismically Isolated Bridges. (Dr.Ing. Thesis)
MTA-92-89	Langli, Geir, MP	Improving Operational Safety through exploitation of Design Knowledge - an investigation of offshore platform safety. (Dr.Ing. Thesis)
MTA-92-90	Sævik, Svein, MK	On Stresses and Fatigue in Flexible Pipes. (Dr.Ing. Thesis)
MTA-92-91	Ask, Tor Ø., MM	Ignition and Flame Growth in Lean Gas-Air Mixtures. An Experimental Study with a Schlieren System. (Dr.Ing. Thesis)
MTA-86-92	Hessen, Gunnar, MK	Fracture Mechanics Analysis of Stiffened Tubular

		Members. (Dr.Ing. Thesis)
MTA-93-93	Steinebach, Christian, MM	Knowledge Based Systems for Diagnosis of Rotating Machinery. (Dr.Ing. Thesis)
MTA-93-94	Dalane, Jan Inge, MK	System Reliability in Design and Maintenance of Fixed Offshore Structures. (Dr.Ing. Thesis)
MTA-93-95	Steen, Sverre, MH	Cobblestone Effect on SES. (Dr.Ing. Thesis)
MTA-93-96	Karunakaran, Daniel, MK	Nonlinear Dynamic Response and Reliability Analysis of Drag-dominated Offshore Platforms. (Dr.Ing. Thesis)
MTA-93-97	Hagen, Arnulf, MP	The Framework of a Design Process Language. (Dr.Ing. Thesis)
MTA-93-98	Nordrik, Rune, MM	Investigation of Spark Ignition and Autoignition in Methane and Air Using Computational Fluid Dynamics and Chemical Reaction Kinetics. A Numerical Study of Ignition Processes in Internal Combustion Engines. (Dr.Ing. Thesis)
MTA-94-99	Passano, Elizabeth, MK	Efficient Analysis of Nonlinear Slender Marine Structures. (Dr.Ing. Thesis)
MTA-94-100	Kvålsvold, Jan, MH	Hydroelastic Modelling of Wetdeck Slamming on Multihull Vessels. (Dr.Ing. Thesis)
MTA-94-102	Bech, Sidsel M., MK	Experimental and Numerical Determination of Stiffness and Strength of GRP/PVC Sandwich Structures. (Dr.Ing. Thesis)
MTA-95-103	Paulsen, Hallvard, MM	A Study of Transient Jet and Spray using a Schlieren Method and Digital Image Processing. (Dr.Ing. Thesis)
MTA-95-104	Hovde, Geir Olav, MK	Fatigue and Overload Reliability of Offshore Structural Systems, Considering the Effect of Inspection and Repair. (Dr.Ing. Thesis)
MTA-95-105	Wang, Xiaozhi, MK	Reliability Analysis of Production Ships with Emphasis on Load Combination and Ultimate Strength. (Dr.Ing. Thesis)
MTA-95-106	Ulstein, Tore, MH	Nonlinear Effects of a Flexible Stern Seal Bag on Cobblestone Oscillations of an SES. (Dr.Ing. Thesis)
MTA-95-107	Solaas, Frøydis, MH	Analytical and Numerical Studies of Sloshing in Tanks. (Dr.Ing. Thesis)
MTA-95-108	Hellan, Øyvind, MK	Nonlinear Pushover and Cyclic Analyses in Ultimate Limit State Design and Reassessment of Tubular Steel Offshore Structures. (Dr.Ing. Thesis)
MTA-95-109	Hermundstad, Ole A., MK	Theoretical and Experimental Hydroelastic Analysis of High Speed Vessels. (Dr.Ing. Thesis)
MTA-96-110	Bratland, Anne K., MH	Wave-Current Interaction Effects on Large-Volume Bodies in Water of Finite Depth. (Dr.Ing. Thesis)

MTA-96-111	Herfjord, Kjell, MH	A Study of Two-dimensional Separated Flow by a Combination of the Finite Element Method and Navier-Stokes Equations. (Dr.Ing. Thesis)
MTA-96-112	Æsøy, Vilmar, MM	Hot Surface Assisted Compression Ignition in a Direct Injection Natural Gas Engine. (Dr.Ing. Thesis)
MTA-96-113	Eknes, Monika L., MK	Escalation Scenarios Initiated by Gas Explosions on Offshore Installations. (Dr.Ing. Thesis)
MTA-96-114	Erikstad, Stein O., MP	A Decision Support Model for Preliminary Ship Design. (Dr.Ing. Thesis)
MTA-96-115	Pedersen, Egil, MH	A Nautical Study of Towed Marine Seismic Streamer Cable Configurations. (Dr.Ing. Thesis)
MTA-97-116	Moksnes, Paul O., MM	Modelling Two-Phase Thermo-Fluid Systems Using Bond Graphs. (Dr.Ing. Thesis)
MTA-97-117	Halse, Karl H., MK	On Vortex Shedding and Prediction of Vortex-Induced Vibrations of Circular Cylinders. (Dr.Ing. Thesis)
MTA-97-118	Igland, Ragnar T., MK	Reliability Analysis of Pipelines during Laying, considering Ultimate Strength under Combined Loads. (Dr.Ing. Thesis)
MTA-97-119	Pedersen, Hans-P., MP	Levendefiskteknologi for fiskefartøy. (Dr.Ing. Thesis)
MTA-98-120	Vikestad, Kyrre, MK	Multi-Frequency Response of a Cylinder Subjected to Vortex Shedding and Support Motions. (Dr.Ing. Thesis)
MTA-98-121	Azadi, Mohammad R. E., MK	Analysis of Static and Dynamic Pile-Soil-Jacket Behaviour. (Dr.Ing. Thesis)
MTA-98-122	Ulltang, Terje, MP	A Communication Model for Product Information. (Dr.Ing. Thesis)
MTA-98-123	Torbergsen, Erik, MM	Impeller/Diffuser Interaction Forces in Centrifugal Pumps. (Dr.Ing. Thesis)
MTA-98-124	Hansen, Edmond, MH	A Discrete Element Model to Study Marginal Ice Zone Dynamics and the Behaviour of Vessels Moored in Broken Ice. (Dr.Ing. Thesis)
MTA-98-125	Videiro, Paulo M., MK	Reliability Based Design of Marine Structures. (Dr.Ing. Thesis)
MTA-99-126	Mainçon, Philippe, MK	Fatigue Reliability of Long Welds Application to Titanium Risers. (Dr.Ing. Thesis)
MTA-99-127	Haugen, Elin M., MH	Hydroelastic Analysis of Slamming on Stiffened Plates with Application to Catamaran Wetdecks. (Dr.Ing. Thesis)
MTA-99-128	Langhelle, Nina K., MK	Experimental Validation and Calibration of Nonlinear Finite Element Models for Use in Design of Aluminium Structures Exposed to Fire. (Dr.Ing.

		Thesis)
MTA-99-129	Berstad, Are J., MK	Calculation of Fatigue Damage in Ship Structures. (Dr.Ing. Thesis)
MTA-99-130	Andersen, Trond M., MM	Short Term Maintenance Planning. (Dr.Ing. Thesis)
MTA-99-131	Tveiten, Bård Wathne, MK	Fatigue Assessment of Welded Aluminium Ship Details. (Dr.Ing. Thesis)
MTA-99-132	Søreide, Fredrik, MP	Applications of underwater technology in deep water archaeology. Principles and practice. (Dr.Ing. Thesis)
MTA-99-133	Tønnessen, Rune, MH	A Finite Element Method Applied to Unsteady Viscous Flow Around 2D Blunt Bodies With Sharp Corners. (Dr.Ing. Thesis)
MTA-99-134	Elvekrok, Dag R., MP	Engineering Integration in Field Development Projects in the Norwegian Oil and Gas Industry. The Supplier Management of Norne. (Dr.Ing. Thesis)
MTA-99-135	Fagerholt, Kjetil, MP	Optimeringsbaserte Metoder for Ruteplanlegging innen skipsfart. (Dr.Ing. Thesis)
MTA-99-136	Bysveen, Marie, MM	Visualization in Two Directions on a Dynamic Combustion Rig for Studies of Fuel Quality. (Dr.Ing. Thesis)
MTA-2000-137	Storteig, Eskild, MM	Dynamic characteristics and leakage performance of liquid annular seals in centrifugal pumps. (Dr.Ing. Thesis)
MTA-2000-138	Sagli, Gro, MK	Model uncertainty and simplified estimates of long term extremes of hull girder loads in ships. (Dr.Ing. Thesis)
MTA-2000-139	Tronstad, Harald, MK	Nonlinear analysis and design of cable net structures like fishing gear based on the finite element method. (Dr.Ing. Thesis)
MTA-2000-140	Kroneberg, André, MP	Innovation in shipping by using scenarios. (Dr.Ing. Thesis)
MTA-2000-141	Haslum, Herbjørn Alf, MH	Simplified methods applied to nonlinear motion of spar platforms. (Dr.Ing. Thesis)
MTA-2001-142	Samdal, Ole Johan, MM	Modelling of Degradation Mechanisms and Stressor Interaction on Static Mechanical Equipment Residual Lifetime. (Dr.Ing. Thesis)
MTA-2001-143	Baarholm, Rolf Jarle, MH	Theoretical and experimental studies of wave impact underneath decks of offshore platforms. (Dr.Ing. Thesis)
MTA-2001-144	Wang, Lihua, MK	Probabilistic Analysis of Nonlinear Wave-induced Loads on Ships. (Dr.Ing. Thesis)
MTA-2001-145	Kristensen, Odd H. Holt, MK	Ultimate Capacity of Aluminium Plates under Multiple Loads, Considering HAZ Properties. (Dr.Ing. Thesis)

MTA-2001-146	Greco, Marilena, MH	A Two-Dimensional Study of Green-Water Loading. (Dr.Ing. Thesis)
MTA-2001-147	Heggelund, Svein E., MK	Calculation of Global Design Loads and Load Effects in Large High Speed Catamarans. (Dr.Ing. Thesis)
MTA-2001-148	Babalola, Olusegun T., MK	Fatigue Strength of Titanium Risers – Defect Sensitivity. (Dr.Ing. Thesis)
MTA-2001-149	Mohammed, Abuu K., MK	Nonlinear Shell Finite Elements for Ultimate Strength and Collapse Analysis of Ship Structures. (Dr.Ing. Thesis)
MTA-2002-150	Holmedal, Lars E., MH	Wave-current interactions in the vicinity of the sea bed. (Dr.Ing. Thesis)
MTA-2002-151	Rognebakke, Olav F., MH	Sloshing in rectangular tanks and interaction with ship motions. (Dr.Ing. Thesis)
MTA-2002-152	Lader, Pål Furset, MH	Geometry and Kinematics of Breaking Waves. (Dr.Ing. Thesis)
MTA-2002-153	Yang, Qinzheng, MH	Wash and wave resistance of ships in finite water depth. (Dr.Ing. Thesis)
MTA-2002-154	Melhus, Øyvin, MM	Utilization of VOC in Diesel Engines. Ignition and combustion of VOC released by crude oil tankers. (Dr.Ing. Thesis)
MTA-2002-155	Ronæss, Marit, MH	Wave Induced Motions of Two Ships Advancing on Parallel Course. (Dr.Ing. Thesis)
MTA-2002-156	Økland, Ole D., MK	Numerical and experimental investigation of whipping in twin hull vessels exposed to severe wet deck slamming. (Dr.Ing. Thesis)
MTA-2002-157	Ge, Chunhua, MK	Global Hydroelastic Response of Catamarans due to Wet Deck Slamming. (Dr.Ing. Thesis)
MTA-2002-158	Byklum, Eirik, MK	Nonlinear Shell Finite Elements for Ultimate Strength and Collapse Analysis of Ship Structures. (Dr.Ing. Thesis)
IMT-2003-1	Chen, Haibo, MK	Probabilistic Evaluation of FPSO-Tanker Collision in Tandem Offloading Operation. (Dr.Ing. Thesis)
IMT-2003-2	Skaugset, Kjetil Bjørn, MK	On the Suppression of Vortex Induced Vibrations of Circular Cylinders by Radial Water Jets. (Dr.Ing. Thesis)
IMT-2003-3	Chezhian, Muthu	Three-Dimensional Analysis of Slamming. (Dr.Ing. Thesis)
IMT-2003-4	Buhaug, Øyvind	Deposit Formation on Cylinder Liner Surfaces in Medium Speed Engines. (Dr.Ing. Thesis)
IMT-2003-5	Tregde, Vidar	Aspects of Ship Design: Optimization of Aft Hull with Inverse Geometry Design. (Dr.Ing. Thesis)
IMT-2003-6	Wist, Hanne Therese	Statistical Properties of Successive Ocean Wave

		Parameters. (Dr.Ing. Thesis)
IMT-2004-7	Ransau, Samuel	Numerical Methods for Flows with Evolving Interfaces. (Dr.Ing. Thesis)
IMT-2004-8	Soma, Torkel	Blue-Chip or Sub-Standard. A data interrogation approach of identity safety characteristics of shipping organization. (Dr.Ing. Thesis)
IMT-2004-9	Ersdal, Svein	An experimental study of hydrodynamic forces on cylinders and cables in near axial flow. (Dr.Ing. Thesis)
IMT-2005-10	Brodtkorb, Per Andreas	The Probability of Occurrence of Dangerous Wave Situations at Sea. (Dr.Ing. Thesis)
IMT-2005-11	Yttervik, Rune	Ocean current variability in relation to offshore engineering. (Dr.Ing. Thesis)
IMT-2005-12	Fredheim, Arne	Current Forces on Net-Structures. (Dr.Ing. Thesis)
IMT-2005-13	Heggernes, Kjetil	Flow around marine structures. (Dr.Ing. Thesis
IMT-2005-14	Fouques, Sebastien	Lagrangian Modelling of Ocean Surface Waves and Synthetic Aperture Radar Wave Measurements. (Dr.Ing. Thesis)
IMT-2006-15	Holm, Håvard	Numerical calculation of viscous free surface flow around marine structures. (Dr.Ing. Thesis)
IMT-2006-16	Bjørheim, Lars G.	Failure Assessment of Long Through Thickness Fatigue Cracks in Ship Hulls. (Dr.Ing. Thesis)
IMT-2006-17	Hansson, Lisbeth	Safety Management for Prevention of Occupational Accidents. (Dr.Ing. Thesis)
IMT-2006-18	Zhu, Xinying	Application of the CIP Method to Strongly Nonlinear Wave-Body Interaction Problems. (Dr.Ing. Thesis)
IMT-2006-19	Reite, Karl Johan	Modelling and Control of Trawl Systems. (Dr.Ing. Thesis)
IMT-2006-20	Smogeli, Øyvind Notland	Control of Marine Propellers. From Normal to Extreme Conditions. (Dr.Ing. Thesis)
IMT-2007-21	Storhaug, Gaute	Experimental Investigation of Wave Induced Vibrations and Their Effect on the Fatigue Loading of Ships. (Dr.Ing. Thesis)
IMT-2007-22	Sun, Hui	A Boundary Element Method Applied to Strongly Nonlinear Wave-Body Interaction Problems. (PhD Thesis, CeSOS)
IMT-2007-23	Rustad, Anne Marthine	Modelling and Control of Top Tensioned Risers. (PhD Thesis, CeSOS)
IMT-2007-24	Johansen, Vegar	Modelling flexible slender system for real-time simulations and control applications
IMT-2007-25	Wroldsen, Anders Sunde	Modelling and control of tensegrity structures. (PhD

		Thesis, CeSOS)
IMT-2007-26	Aronsen, Kristoffer Høye	An experimental investigation of in-line and combined inline and cross flow vortex induced vibrations. (Dr. avhandling, IMT)
IMT-2007-27	Gao, Zhen	Stochastic Response Analysis of Mooring Systems with Emphasis on Frequency-domain Analysis of Fatigue due to Wide-band Response Processes (PhD Thesis, CeSOS)
IMT-2007-28	Thorstensen, Tom Anders	Lifetime Profit Modelling of Ageing Systems Utilizing Information about Technical Condition. (Dr.ing. thesis, IMT)
IMT-2008-29	Berntsen, Per Ivar B.	Structural Reliability Based Position Mooring. (PhD-Thesis, IMT)
IMT-2008-30	Ye, Naiquan	Fatigue Assessment of Aluminium Welded Box-stiffener Joints in Ships (Dr.ing. thesis, IMT)
IMT-2008-31	Radan, Damir	Integrated Control of Marine Electrical Power Systems. (PhD-Thesis, IMT)
IMT-2008-32	Thomassen, Paul	Methods for Dynamic Response Analysis and Fatigue Life Estimation of Floating Fish Cages. (Dr.ing. thesis, IMT)
IMT-2008-33	Pákozdi, Csaba	A Smoothed Particle Hydrodynamics Study of Two-dimensional Nonlinear Sloshing in Rectangular Tanks. (Dr.ing.thesis, IMT)
IMT-2007-34	Grytøyr, Guttorm	A Higher-Order Boundary Element Method and Applications to Marine Hydrodynamics. (Dr.ing.thesis, IMT)
IMT-2008-35	Drummen, Ingo	Experimental and Numerical Investigation of Nonlinear Wave-Induced Load Effects in Containerships considering Hydroelasticity. (PhD thesis, CeSOS)
IMT-2008-36	Skejic, Renato	Maneuvering and Seakeeping of a Singel Ship and of Two Ships in Interaction. (PhD-Thesis, CeSOS)
IMT-2008-37	Harlem, Alf	An Age-Based Replacement Model for Repairable Systems with Attention to High-Speed Marine Diesel Engines. (PhD-Thesis, IMT)
IMT-2008-38	Alsos, Hagbart S.	Ship Grounding. Analysis of Ductile Fracture, Bottom Damage and Hull Girder Response. (PhD-thesis, IMT)
IMT-2008-39	Graczyk, Mateusz	Experimental Investigation of Sloshing Loading and Load Effects in Membrane LNG Tanks Subjected to Random Excitation. (PhD-thesis, CeSOS)
IMT-2008-40	Taghipour, Reza	Efficient Prediction of Dynamic Response for Flexible amd Multi-body Marine Structures. (PhD-thesis, CeSOS)
IMT-2008-41	Ruth, Eivind	Propulsion control and thrust allocation on marine vessels. (PhD thesis, CeSOS)

IMT-2008-42	Nystad, Bent Helge	Technical Condition Indexes and Remaining Useful Life of Aggregated Systems. PhD thesis, IMT
IMT-2008-43	Soni, Prashant Kumar	Hydrodynamic Coefficients for Vortex Induced Vibrations of Flexible Beams, PhD thesis, CeSOS
IMT-2009-43	Amlashi, Hadi K.K.	Ultimate Strength and Reliability-based Design of Ship Hulls with Emphasis on Combined Global and Local Loads. PhD Thesis, IMT
IMT-2009-44	Pedersen, Tom Arne	Bond Graph Modelling of Marine Power Systems. PhD Thesis, IMT
IMT-2009-45	Kristiansen, Trygve	Two-Dimensional Numerical and Experimental Studies of Piston-Mode Resonance. PhD-Thesis, CeSOS
IMT-2009-46	Ong, Muk Chen	Applications of a Standard High Reynolds Number Model and a Stochastic Scour Prediction Model for Marine Structures. PhD-thesis, IMT
IMT-2009-47	Hong, Lin	Simplified Analysis and Design of Ships subjected to Collision and Grounding. PhD-thesis, IMT
IMT-2009-48	Koushan, Kamran	Vortex Induced Vibrations of Free Span Pipelines, PhD thesis, IMT
IMT-2009-49	Korsvik, Jarl Eirik	Heuristic Methods for Ship Routing and Scheduling. PhD-thesis, IMT
IMT-2009-50	Lee, Jihoon	Experimental Investigation and Numerical in Analyzing the Ocean Current Displacement of Longlines. Ph.d.-Thesis, IMT.
IMT-2009-51	Vestbøstad, Tone Gran	A Numerical Study of Wave-in-Deck Impact usin a Two-Dimensional Constrained Interpolation Profile Method, Ph.d.thesis, CeSOS.
IMT-2009-52	Bruun, Kristine	Bond Graph Modelling of Fuel Cells for Marine Power Plants. Ph.d.-thesis, IMT
IMT 2009-53	Holstad, Anders	Numerical Investigation of Turbulence in a Sekwed Three-Dimensional Channel Flow, Ph.d.-thesis, IMT.
IMT 2009-54	Ayala-Uraga, Efren	Reliability-Based Assessment of Deteriorating Ship-shaped Offshore Structures, Ph.d.-thesis, IMT
IMT 2009-55	Kong, Xiangjun	A Numerical Study of a Damaged Ship in Beam Sea Waves. Ph.d.-thesis, IMT/CeSOS.
IMT 2010-56	Kristiansen, David	Wave Induced Effects on Floaters of Aquaculture Plants, Ph.d.-thesis, IMT/CeSOS.
IMT 2010-57	Ludvigsen, Martin	An ROV-Toolbox for Optical and Acoustic Scientific Seabed Investigation. Ph.d.-thesis IMT.
IMT 2010-58	Hals, Jørgen	Modelling and Phase Control of Wave-Energy Converters Ph.d.thesis, CeSOS.

IMT 2010-59	Shu, Zhi	Uncertainty Assessment of Wave Loads and Ultimate Strength of Tankers and Bulk Carriers in a Reliability Framwork. Ph.d. Thesis, IMT.
IMT 2010-60	Jakobsen, Ken-Robert	Turbulence Modeling of Transverse Flow on Ships in Shallow Water. Ph.D.Thesis IMT.
IMT 2010-61	Shao, Yanlin	Numerical Potential-Flow Studies on Weakly-Nonlinear Wave-Body Interaction with/without Small Forward Speed. Ph.d. Thesis, IMT.